JEM Journal of Experimental Medicine

BRIEF DEFINITIVE REPORT

Eosinophils are part of the granulocyte response in tuberculosis and promote host resistance in mice

Andrea C. Bohrer[1*], Ehydel Castro[1*], Zhidong Hu[2,3*], Artur T.L. Queiroz[4], Claire E. Tocheny[1], Maike Assmann[1], Shunsuke Sakai[5], Christine Nelson[5], Paul J. Baker[1], Hui Ma[2,3], Lin Wang[3,6], Wen Zilu[3,6], Elsa du Bruyn[7], Catherine Riou[7], Keith D. Kauffman[5], Tuberculosis Imaging Program[8], Ian N. Moore[9], Franca Del Nonno[10], Linda Petrone[11], Delia Goletti[11], Adrian R. Martineau[12], David M. Lowe[12], Mark R. Cronan[13,14], Robert J. Wilkinson[7,15,16], Clifton E. Barry III[7,17], Laura E. Via[8,17], Daniel L. Barber[5], Amy D. Klion[18], Bruno B. Andrade[4], Yanzheng Song[3,6], Ka-Wing Wong[2,3], and Katrin D. Mayer-Barber[1]

Host resistance to *Mycobacterium tuberculosis* (*Mtb*) infection requires the activities of multiple leukocyte subsets, yet the roles of the different innate effector cells during tuberculosis are incompletely understood. Here we uncover an unexpected association between eosinophils and *Mtb* infection. In humans, eosinophils are decreased in the blood but enriched in resected human tuberculosis lung lesions and autopsy granulomas. An influx of eosinophils is also evident in infected zebrafish, mice, and nonhuman primate granulomas, where they are functionally activated and degranulate. Importantly, using complementary genetic models of eosinophil deficiency, we demonstrate that in mice, eosinophils are required for optimal pulmonary bacterial control and host survival after *Mtb* infection. Collectively, our findings uncover an unexpected recruitment of eosinophils to the infected lung tissue and a protective role for these cells in the control of *Mtb* infection in mice.

Introduction

Mycobacterium tuberculosis (*Mtb*) is an intracellular bacterium that causes tuberculosis (TB), which through 2020 accounted for the highest yearly global mortality due to a single pathogen (World Health Organization, 2020). *Mtb* primarily infects innate immune cells, and host resistance depends on antimicrobial effector functions of infected macrophages alongside a robust type I and T helper 1 cell immune response (Cooper et al., 1993; Ernst, 2012; Flynn et al., 1993; Flynn et al., 2015). Eosinophils, in contrast, are major innate effector cells in type II inflammatory settings (Klion and Nutman, 2004; Simon et al., 2020). Accordingly, reports of type II immunity-associated cells and responses during *Mtb* infection are rare, with one report of eosinophils in lungs of *Mtb*-infected guinea pigs (Lasco et al., 2004) and one case series of pulmonary eosinophilia in three TB patients (Vijayan et al., 1992). As a result, eosinophils have been assumed to be largely uninvolved in the immune response to *Mtb* or actively repressed by the strong IFN-γ–driven responses required for control of mycobacteria (Cooper et al., 1993; Flynn and Ernst, 2000; Kirman et al., 2000; O'Garra et al., 2013).

Studies of eosinophil responses in vivo have historically focused on allergic responses and parasitic helminth infections (Klion et al., 2020; Travers and Rothenberg, 2015). Eosinophils are associated with an established type II response during lung infections with respiratory syncytial virus and *Aspergillus* (Lilly

[1]Inflammation and Innate Immunity Unit, Laboratory of Clinical Immunology and Microbiology, National Institute of Allergy and Infectious Diseases, National Institutes of Health, Bethesda, MD; [2]Department of Scientific Research, Shanghai Public Health Clinical Center, Fudan University, Shanghai, China; [3]Tuberculosis Center, Shanghai Emerging and Re-emerging Infectious Disease Institute, Fudan University, Shanghai, China; [4]The KAB group, Multinational Organization Network Sponsoring Translational and Epidemiological Research Initiative, Instituto Gonçalo Moniz, Fundação Oswaldo Cruz, Salvador Brazil; [5]T Lymphocyte Biology Section, Laboratory of Parasitic Diseases, National Institute of Allergy and Infectious Diseases, National Institutes of Health, Bethesda, MD; [6]Department of Thoracic Surgery, Shanghai Public Health Clinical Center, Fudan University, Shanghai, China; [7]Wellcome Centre for Infectious Diseases Research in Africa, Institute of Infectious Disease and Molecular Medicine, University of Cape Town, South Africa; [8]Tuberculosis Imaging Program, Division of Intramural Research, National Institute of Allergy and Infectious Diseases, National Institutes of Health, Bethesda, MD; [9]Infectious Disease Pathogenesis Section, Comparative Medicine Branch, National Institute of Allergy and Infectious Diseases, National Institutes of Health, Bethesda, MD; [10]Pathology Unit, National Institute for Infectious Diseases "L. Spallanzani," Istituto Di Ricovero e Cura a Carattere Scientifico, Rome, Italy; [11]Translational Research Unit, Department of Epidemiology and Preclinical Research National Institute for Infectious Diseases, Istituto Di Ricovero e Cura a Carattere Scientifico, Rome, Italy; [12]Institute of Immunity and Transplantation, University College London, London, UK; [13]In Vivo Cell Biology of Infection Unit, Max Planck Institute for Infection Biology, Berlin, Germany; [14]Department of Molecular Genetics and Microbiology, Duke University School of Medicine, Durham, NC; [15]Department of Infectious Diseases, Imperial College London, UK; [16]Francis Crick Institute, London, UK; [17]Tuberculosis Research Section, Laboratory of Clinical Immunology and Microbiology, National Institute of Allergy and Infectious Diseases, National Institutes of Health, Bethesda, MD; [18]Human Eosinophil Section, Laboratory of Parasitic Diseases, National Institute of Allergy and Infectious Diseases, National Institutes of Health, Bethesda, MD.

*A.C. Bohrer, E. Castro, and Z. Hu contributed equally to this paper; Correspondence to Katrin D. Mayer-Barber: mayerk@niaid.nih.gov; Ka-Wing Wong: kwwong@gmail.com.

et al., 2014; Phipps et al., 2007), and recent data have highlighted complex roles for eosinophils in tissue homeostasis and remodeling, barrier function, and wound healing (Lee et al., 2010; Rosenberg et al., 2013; Shah et al., 2020). Indeed, eosinophils are pluripotent, armed with a variety of bioactive molecules stored preformed in granules or synthesized in lipid bodies. These include a large repertoire of cytokines, chemokines, lipid mediators, and cationic granule proteins, including eosinophil cationic protein, eosinophil-derived neurotoxin, eosinophil peroxidase (EPX), and major basic protein (Acharya and Ackerman, 2014; Klion et al., 2020; Shamri et al., 2011). However, our understanding of the in vivo function of eosinophils during bacterial infections is limited. Reports are currently restricted to extracellular bacteria where direct cell-autonomous bactericidal properties of eosinophils, including extracellular DNA traps and bactericidal granule proteins, can promote extracellular clearance of *Escherichia coli*, *Citrobacter rodentium*, *Staphylococcus aureus*, and *Pseudomonas aeruginosa* bacteria (Arnold et al., 2018; Krishack et al., 2019; Linch et al., 2009; Yousefi et al., 2008). However, the physiological role of eosinophils in host resistance to intracellular bacterial infections remains unknown.

Here we establish that eosinophils are a significant cellular component of TB granulomas and *Mtb*-infected lungs in mice, nonhuman primates (NHPs), and patients. Using complementary genetic approaches to create eosinophil deficiency, we demonstrate that eosinophil responses are required for optimal host resistance and survival after *Mtb* infection in mice. Together, our findings reveal a previously unrecognized association between eosinophils and TB in multiple hosts and uncover a protective role for these cells in mice.

Results and discussion

We started by investigating whether eosinophils participated in the granulocytic response to TB by quantifying circulating eosinophils in three independent clinical cohort studies (Du Bruyn et al., 2021; Lowe et al., 2013; Mayer-Barber et al., 2014). We asked whether the numbers of peripheral blood eosinophils of TB patients changed based on disease status and antitubercular treatment (ATT) in a South African cohort (Du Bruyn et al., 2021). Indeed, blood eosinophil numbers were significantly higher in individuals with latent TB infection (LTBI) compared with active pulmonary TB (PTB) patients (Fig. 1 A), with a corresponding decreased eosinophil-to-neutrophil (E/N) ratio in the PTB group (Fig. S1, A and B). When patients in an independent Chinese cohort (Mayer-Barber et al., 2014) were stratified according to disease severity based on sputum positivity for acid-fast staining of bacilli (AFB), individuals with active AFB$^+$ PTB and extrapulmonary TB (EPTB) disease exhibited a significantly decreased E/N ratio compared with AFB$^-$ PTB patients (Fig. S1 C). These data suggest that a decrease in circulating E/N ratio may reflect an increase in sputum bacterial loads. Consistent with the hypothesis that blood eosinophil numbers reflect bacterial sputum status and disease burden, circulating blood eosinophil numbers increased significantly within 2 wk of commencing ATT in both cohorts (Fig. 1 B and Fig. S1 D). Moreover, in a third British cohort that included patients with both PTB and EPTB (Lowe et al., 2013), TB disease survivors exhibited a significantly higher E/N ratio on blood tests taken at the time of diagnosis compared with individuals who subsequently died (Fig. S1 E). In fact, lower baseline eosinophil numbers in blood correlated with shorter time to TB-related death (Fig. S1 F). Taken together, our data from three independent clinical cohorts suggest that peripheral blood eosinophils are decreased according to disease severity, raising the possibility that rather than being depleted, eosinophils may be recruited to distant disease sites where they could participate in the local immune response to infection.

To directly address whether eosinophils could be part of the local pulmonary granulocyte response in human TB, we measured the relative abundance of granulocytes in human TB lesions. To this end, we generated single-cell suspensions from freshly resected human lung tissue (n = 9 TB patients) directly after clinically indicated surgery and identified tissue-resident granulocytes with established markers Siglec-8$^+$/CD66b$^+$ for eosinophils and Siglec-8$^-$/CD66b$^+$ for neutrophils (Fig. 1 C and Fig. S1 G). Neutrophils were abundant CD45$^+$ immune cells in human lung lesions divided into different macropathologies (Fig. S1 H). However, eosinophils were also frequently present in appreciable numbers relative to neutrophils in the same lung lesion sample (Fig. 1 D and Fig. S1 H). In fact, E/N ratios and eosinophil frequencies of CD45$^+$ immune cells were sometimes similar to or even higher than neutrophils in some, but not all, samples from fibrotic areas and granulomas compared with the blood in the same individuals (Fig. 1, D and E; and Fig. S1, H and I). We then asked whether eosinophils would selectively infiltrate metabolically active inflamed lung lesions via 2-deoxy-2-fluorine-18-fluoro-D-glucose (^{18}FDG) positron emission tomography (PET)/computed tomography (CT) since the more recent patients received ^{18}FDG PET/CT scans to aid in defining the surgical regions before resection. When we separated individual lesions based on high or low metabolic activity via ^{18}FDG signal intensity, eosinophils were significantly increased relative to neutrophils in PET-high compared with PET-low lung lesions (Fig. 1 F and Fig. S1 J). These data suggest that eosinophils are more abundant in PET FDG-avid areas compared with areas of low metabolic activity and disease. While larger studies are needed to accurately categorize and associate the abundance of specific granulocyte subsets within diverse TB lesion types, our small retrospective study showed that eosinophils can be substantially enriched in individual human TB lesions. Most importantly, the E/N ratio was significantly higher in resected human lung lesion types compared with circulation in the same patients (Fig. 1 G), supporting our hypothesis that peripheral blood eosinophils decrease during active TB disease and enrich at infected tissue sites. While a functional role for eosinophils in human disease remains unclear, our clinical data support the hypothesis that during TB, circulating peripheral blood eosinophils are dynamically regulated based on disease status and that eosinophils can be enriched at the *Mtb*-infected local tissue site.

To confirm the flow cytometric data, we next examined human TB granuloma sections from an independent autopsy cohort (Fig. 2 A; Blauenfeldt et al., 2018). H&E staining indicated that eosinophils were present primarily in the rim area of the granulomas (Fig. S2 A), whereas diffuse staining for the eosinophil granule protein EPX was observed in the necrotic core of

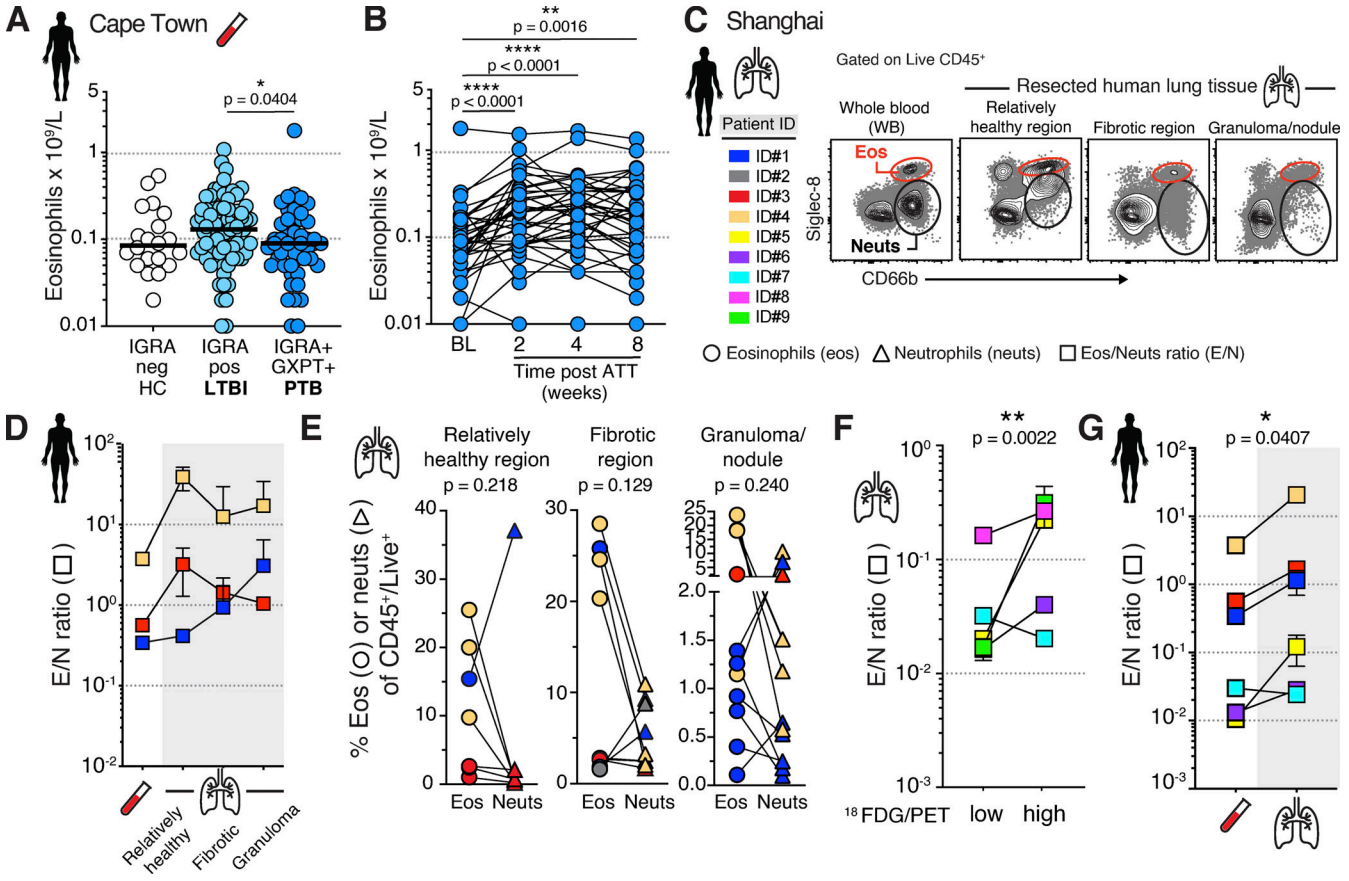

Figure 1. **Eosinophils are decreased in circulation and enriched in human lung lesions during TB. (A)** Cape Town cohort: Circulating eosinophil and neutrophil numbers in HC (n = 20), IGRA-positive individuals with LTBI (n = 77) and IGRA-positive and GXPT-positive PTB (n = 48; Kruskal–Wallis test with Dunn's correction). **(B)** Cape Town cohort: Circulating eosinophil numbers at baseline (BL) and after ATT (n = 37; two-tailed Wilcoxon matched pairs test). **(C)** Shanghai cohort: Representative FACS plots (from participant ID#1) of granulocytes in WB and resected human TB lesions (n = 9; color coded). **(D)** Shanghai cohort: Summary E/N ratios in resected human lung lesions (connecting line according to color-coded patient ID; tissues are depicted as mean and SEM of n = 1–6 samples per tissue type and patient). **(E)** Shanghai cohort: Eosinophil and neutrophil proportions of CD45⁺ cells depicting individual samples per patient (connecting line according to color-coded patient ID, two-tailed Wilcoxon matched pairs test). **(F)** Shanghai cohort: E/N ratios in ^{18}FDG PET/CT low- or high-signal intensity (SUV_{max} >5.0) lung lesions (connecting line according to color-coded patient ID, n = 5, two-tailed ratio paired t test). **(G)** Shanghai cohort: Summary E/N ratios in combined resected human lung lesions (n = 3–22) per patient (n = 6) compared with patients' blood eosinophils (connecting line according to color-coded patient ID, two-tailed ratio paired t test).

granulomas, suggesting eosinophil degranulation in the center of TB granulomas (Fig. 2 A and Fig. S2 A). To experimentally explore the role of eosinophils, we employed an NHP model in which *Mtb* infection forms bona fide lung granuloma structures closely resembling those found in humans (Basaraba and Hunter, 2017; Flynn et al., 2015). We initially assessed lung granulomas from *Mtb*-infected macaques at 7–12 wk after infection for eosinophil infiltration (Fig. S2 B). Like the human TB granulomas, eosinophils were evident in the outer rim area in addition to more diffuse EPX staining in the necrotic core of some granulomas, suggesting degranulated eosinophils (Fig. 2 B; and Fig. S2, C and D). We then asked whether eosinophil recruitment to mycobacterial granulomas was an evolutionarily conserved process. Using the zebrafish model, we assessed eosinophils in mycobacterial granulomas formed after *Mycobacterium marinum* infection (Parikka et al., 2012; Swaim et al., 2006). Indeed, in agreement with our findings in NHP and human TB granulomas, eosinophils were also found in necrotic granulomas in *M. marinum*–infected zebrafish (Fig. 2 C). Taken together, our data show that eosinophils are present in mycobacterial granulomas in human, NHP, and zebrafish, suggesting that infiltration of eosinophils into granulomas may be a conserved response to mycobacteria across species.

To measure eosinophil activation and infiltration into granulomas, we examined NHP granulomas in greater detail. To quantify and functionally assess eosinophils at the single-cell level in rhesus macaques, we developed a flow cytometric approach based on EPX (Fig. S2 E). We found that intracellular staining with EPX selectively and specifically stained eosinophils in whole blood (WB) as well as in bronchoalveolar lavage (BAL) fluid (Fig. 3 A). Importantly, when we quantified eosinophils in NHP TB granulomas, we observed a high level of heterogeneity between individual granulomas with eosinophils spanning four orders of magnitude, comprising up to 10% of all CD45⁺ immune cells with an average of 1.5% in 46 granulomas from seven animals (Fig. 3 B and Fig. S2 F). There was no correlation between

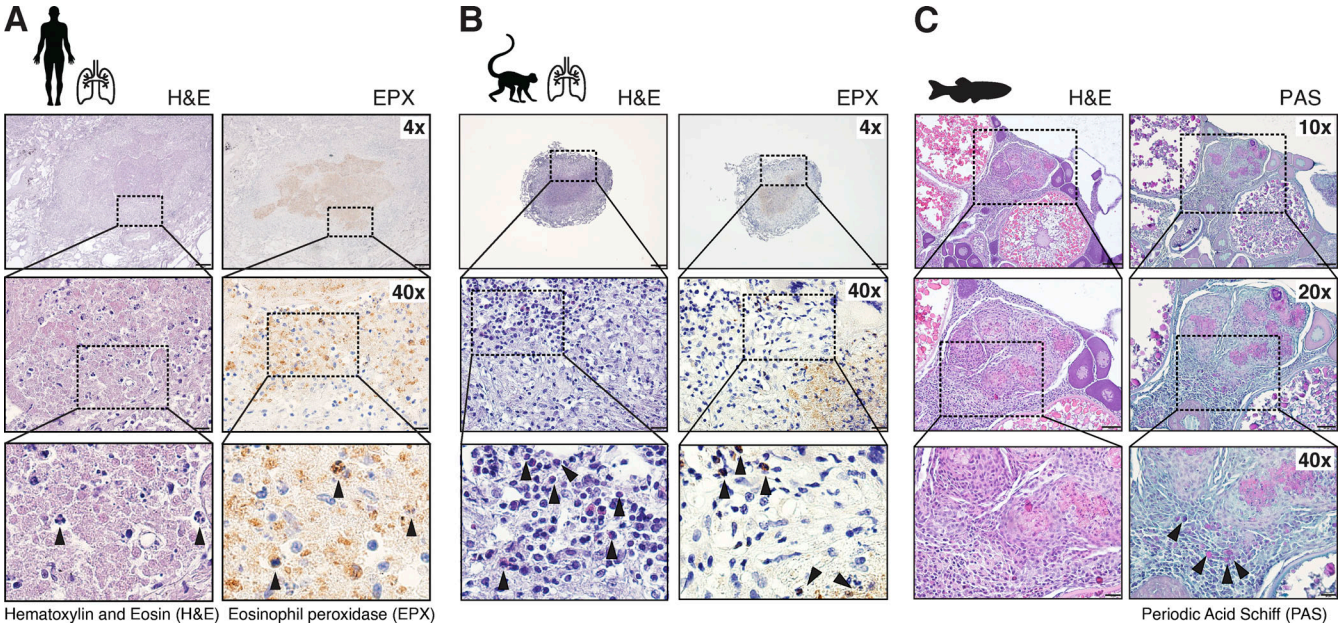

Figure 2. **The presence of eosinophils in mycobacterial granulomas is evolutionarily conserved. (A)** Rome cohort: H&E and EPX immunostaining of paraffin-embedded human *Mtb* lung lesions; arrowheads indicate eosinophils. **(B)** H&E and EPX immunostaining of paraffin-embedded rhesus macaque *Mtb* granulomas; arrowheads indicate eosinophils. **(C)** Organized core of a multifocal granuloma in the ovary of an *M. marinum*–infected zebrafish; arrowheads indicate individual eosinophils stained by PAS in the rim of the granuloma. Scale bars = 200 µm (4×), 100 µm (10×), 50 µm (20×), and 20 µm (40×).

individual granuloma bacterial loads and eosinophil abundance (Fig. 3 C). Since diffuse EPX staining in the core of human and NHP granulomas was suggestive of functional activation resulting in degranulation, we next quantified eosinophil degranulation by measuring CD63 surface expression (Fig. 3 D). While blood eosinophils showed little change in CD63 expression, BAL and granuloma eosinophils exhibited significantly increased CD63 expression, with the highest CD63 expression in granulomas (Fig. 3 D). The proportion of $CD63^+$ eosinophils varied widely between individual granulomas, even within the same animal, and was strongly negatively correlated with the abundance of eosinophils (Fig. 3 E), supporting the idea that eosinophil degranulation precedes cell death. Importantly, CD63 expression on eosinophils inversely correlated with bacterial burden in granulomas (Fig. 3 F), suggesting that functional activation of eosinophils in the form of degranulation may impact bacterial growth in *Mtb* lesions. Collectively, our data from *Mtb*-infected NHP lesions reveal a high degree of heterogeneity in the eosinophilic response and support the hypothesis that eosinophils migrate into TB granulomas where they degranulate and participate in the local innate immune response against *Mtb*.

As a next step in examining the function of eosinophils during *Mtb* infection, we quantified eosinophils after low-dose aerosol *Mtb* infection in the genetically tractable C57BL/6 mouse model (B6). We measured lung tissue resident eosinophils by flow cytometry using an i.v. labeling technique that distinguishes between cells located in the lung vascular capillary bed ($i.v.^{pos}$) and cells that migrated into the lung tissue parenchyma ($i.v.^{neg}$; Anderson et al., 2014). When we quantified the number of lung tissue–resident $i.v.^{neg}$ eosinophils after *Mtb* infection, we observed an increase after 2–3 mo of *Mtb* infection compared with either uninfected animals or 30 d postinfection (d30pi; Fig. 4 A; and Fig. S3, A and B). To ask whether eosinophils could be directly harboring *Mtb*, either by infection or phagocytosis, we assessed bacteria-containing eosinophils using fluorescent *Mtb*-mCherry and found that eosinophils are not infected with *Mtb* (Fig. 4 B). In fact, *Mtb*-infected cells have been identified and described in detail (Cohen et al., 2018; Huang et al., 2018; Lee et al., 2020; Pisu et al., 2020; Rothchild et al., 2019; Wolf et al., 2007), and we, like others, have consistently failed to detect significant numbers of *Mtb*-containing eosinophils (Lee et al., 2020; Rothchild et al., 2019). Thus, while eosinophils may interact with *Mtb* or *Mtb*-infected cells in lungs and TB granulomas, they themselves do not appear to represent a cellular niche for *Mtb*. Based on the increase in lung parenchymal eosinophils after infection and their role in tissue homeostasis (Lee et al., 2010; Rosenberg et al., 2013; Shah et al., 2020), we asked whether the absence of eosinophils after *Mtb* infection would lead to noticeable changes in lung pathology. To this end, we infected B6 ΔdblGata mice that lack eosinophils due to a targeted deletion of a high-affinity GATA–binding site in the GATA-1 promoter (Yu et al., 2002). However, we did not observe changes in lung gross pathology 3 mo after *Mtb* infection in B6 ΔdblGata compared with WT mice (Fig. 4 C). We then examined lung-resident immune cells and found no changes in $i.v.^{neg}$ *Mtb*-specific $CD4^+$ and $CD8^+$ T cells (Fig. S3, C–F), $NK1.1^+$ cells (Fig. S3 G), neutrophils (Fig. S3 H), interstitial macrophage/dendritic cell (DC) polarization states (Fig. S3 I), alveolar macrophages (Fig. S3 J), or $XCR1^+$ DC1 (Fig. S3 K) in B6 ΔdblGata mice compared with WT mice 3 mo after *Mtb* infection. Finally, to explore the impact of eosinophil deficiency in an unbiased fashion, we performed whole-lung transcriptional profiling on 3-mo

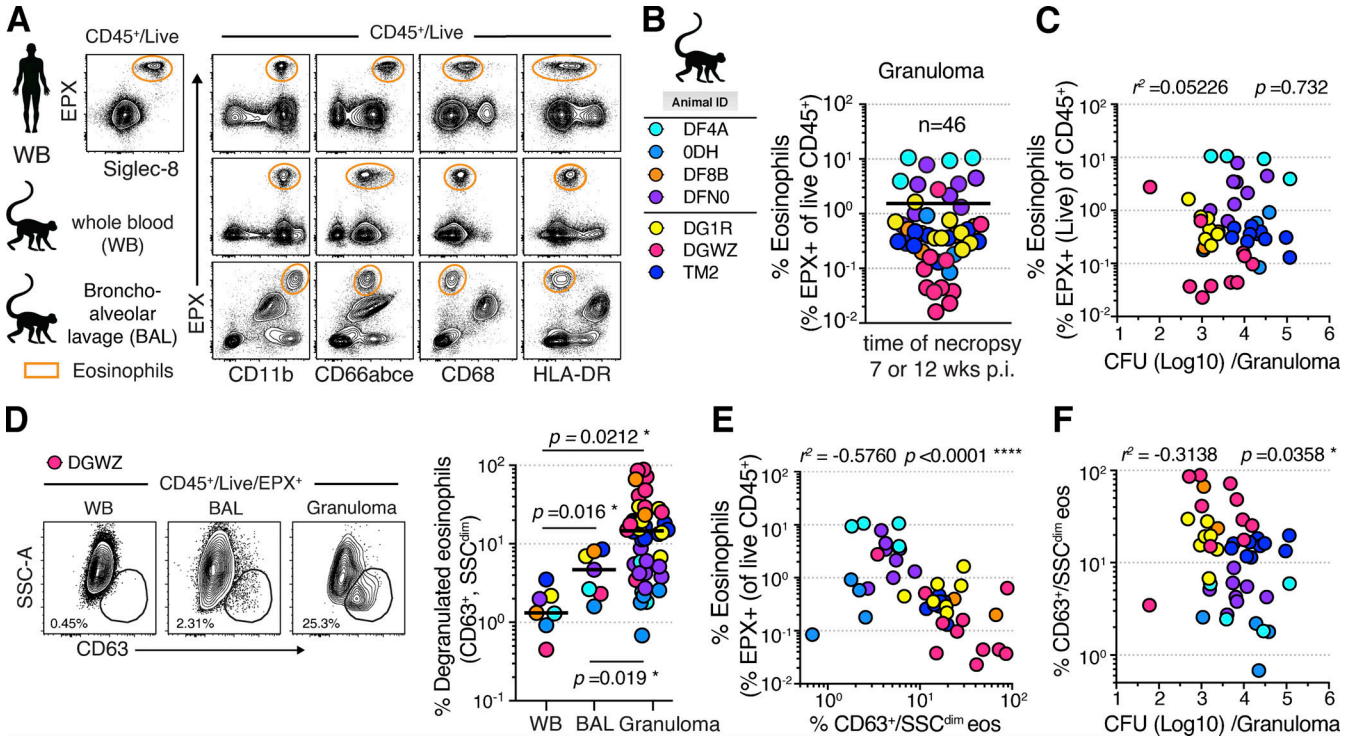

Figure 3. **Eosinophils infiltrate and degranulate in *Mtb* granulomas of rhesus macaques. (A)** Representative FACS plots of EPX staining of eosinophils in WB from healthy donors and uninfected rhesus macaques WB and BAL. **(B)** Animal ID list and corresponding color code of *Mtb* infections in the present study (two independent studies, n = 3–4, male and female) and percentage of eosinophils in pulmonary *Mtb* granulomas (n = 46). **(C)** Correlation plot of eosinophil frequency and granuloma *Mtb* CFU (Spearman correlation test). **(D)** Left: Representative FACS plots of eosinophil CD63 surface expression to quantify degranulation in indicated tissues. Right: Summary data on frequency of degranulated eosinophils per individual granuloma (n = 46; Wilcoxon matched pairs test for WB and BAL comparison and two-tailed ratio matched paired t test for granuloma comparisons). **(E)** Correlation plot of frequency of CD63⁺ eosinophils and eosinophil abundance (Spearman correlation test). **(F)** Correlation plot of frequency of CD63⁺ eosinophils and granuloma *Mtb* CFU (Spearman correlation test). eos, eosinophil; p.i., postinfection; SSC, side scatter.

Mtb-infected B6 ΔdblGata or WT mice alongside day 0 (d0) uninfected controls. Relatively few genes were significantly and differentially expressed when we directly compared transcripts from d90pi B6 ΔdblGata and d90pi WT mouse lungs. 16 differentially expressed genes (DEGs) were upregulated and 9 downregulated in *Mtb*-infected ΔdblGata lungs compared with *Mtb*-infected B6 control lungs (Fig. S3 L). Intriguingly, most of these DEGs were not associated with immunity to infection but, instead, were linked to neurological disorders and neuronal pathways (Fig. S3 L, pink annotation). To explore infection-induced changes, we analyzed and compared d90pi B6 ΔdblGata and d90pi WT mouse lungs with d0 WT controls. We identified 194 up- and 262 downregulated DEGs in *Mtb*-infected ΔdblGata lungs alongside 94 up- and 230 downregulated DEGs in *Mtb*-infected WT B6 lungs (Fig. S3 M). The top 20 DEGs were again enriched in neuronal-, sensory-, and olfactory-associated genes (pink annotation) in addition to genes related to lipid metabolism (green annotation; Fig. 4 D). Consistent with limited changes in genes linked to host resistance, transcriptional module exploration for type I and type II IFNs (Singhania et al., 2019) confirmed the restricted molecular perturbations in *Mtb*-infected eosinophil-deficient compared with WT lungs (Table S1). Importantly, gene set enrichment analyses (GSEAs) revealed again downregulation of pathways associated with neuronal processes; neurological disorders; and short-chain fatty acid, endocannabinoid, and arachidonic acid metabolism in the lungs of *Mtb*-infected ΔdblGata mice (Fig. 4 E and Table S1). Eosinophils produce a variety of bioactive arachidonic acid–derived lipid mediators, some of which have been implicated in host resistance to *Mtb* infection before (Mayer-Barber and Sher, 2015). Furthermore, endocannabinoids and arachidonic acid derivatives interact with sensory neurons in the airways (Bozkurt, 2019; Chesné et al., 2019). One possible interpretation of the neuronal-associated transcriptional changes could be that they reflect alterations in airway sensory neurons or pulmonary neuroendocrine cells of the lung epithelium. Thus, while our transcriptional profiling of *Mtb*-infected lungs revealed neuronal-associated pathways as being primarily affected by the lack of eosinophils, the biological significance of these transcriptional changes remains unknown. Moreover, the pulmonary–neuronal axis in host resistance against *Mtb* infection is largely unexplored, yet there is growing appreciation for the importance of the crosstalk between the nervous and immune systems (Veiga-Fernandes and Mucida, 2016). For instance, a recent study found that *Mtb*-derived sulfolipids can directly bind and activate nociceptive neurons in the lung (Ruhl et al., 2020). Eosinophils have been further shown to alter parasympathetic nerve function and airway sensory nerve density, thereby affecting reflex bronchoconstriction in asthma (Costello

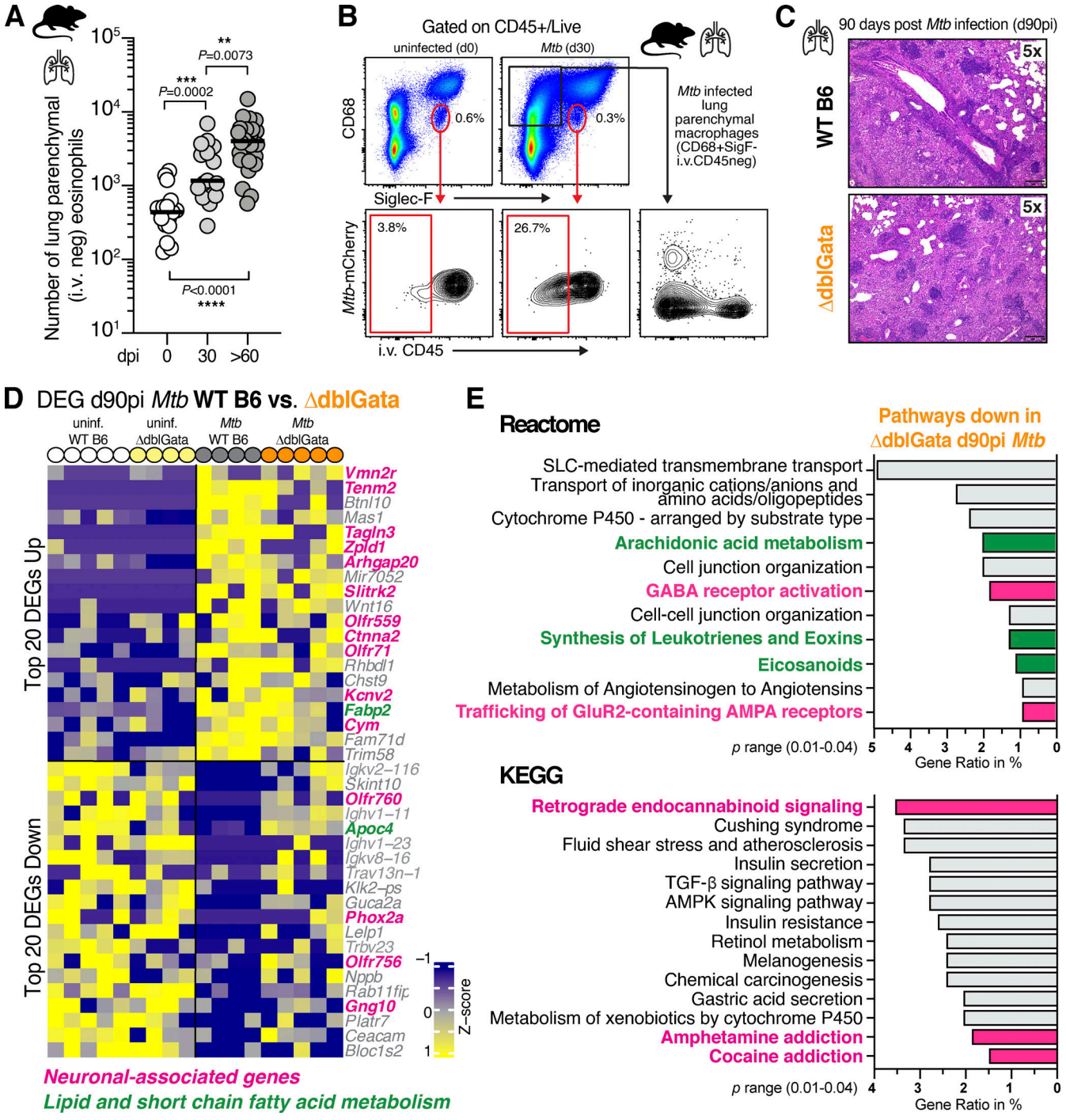

Figure 4. **Pulmonary transcriptional profiling of *Mtb*-infected eosinophil-deficient mice reveals perturbations in lung neuronal-associated pathways. (A)** Cell number of lung parenchymal (CD45 i.v.^{neg}) eosinophils over time after standard low-dose (100–300 CFU aerosol *Mtb* H37Rv infection in B6 mice, male and female, *n* = 12–25 per time point, three to four independent experiments, Mann–Whitney test). **(B)** Representative FACS plots of i.v. staining and *Mtb*–mCherry quantification of eosinophils in the lungs of B6 WT mice after *Mtb* aerosol infection at d30 (three to four independent experiments). **(C)** Representative sections of H&E staining from paraffin-embedded lungs of *Mtb*-infected (d90) WT or B6 ΔdblGata mice (male and female, *n* = 5–6, two independent experiments). Scale bars = 250 µm (5×). **(D)** Heatmap of top 20 upregulated and top 20 downregulated DEGs of d90 WT compared with d90 B6 ΔdblGata normalized to uninfected (uninf.) WT mice (female, *n* = 4–5, one experiment). Neuronal-associated genes are highlighted in pink; lipid and short-chain fatty acid metabolism are highlighted in green. **(E)** GSEA based on Reactome and Kyoto Encyclopedia of Genes and Genomes (KEGG) of key pathways that are selectively downregulated in d90 B6 ΔdblGata mice. Neuronal-associated pathways are highlighted in pink; lipid and short-chain fatty acid metabolism pathways are highlighted in green. AMPA, α-amino-3-hydroxy-5-methyl-4-isoxazolepropionic acid; AMPK, AMP-activated protein kinase; GABA, γ-aminobutyric acid; SLC, solute carrier.

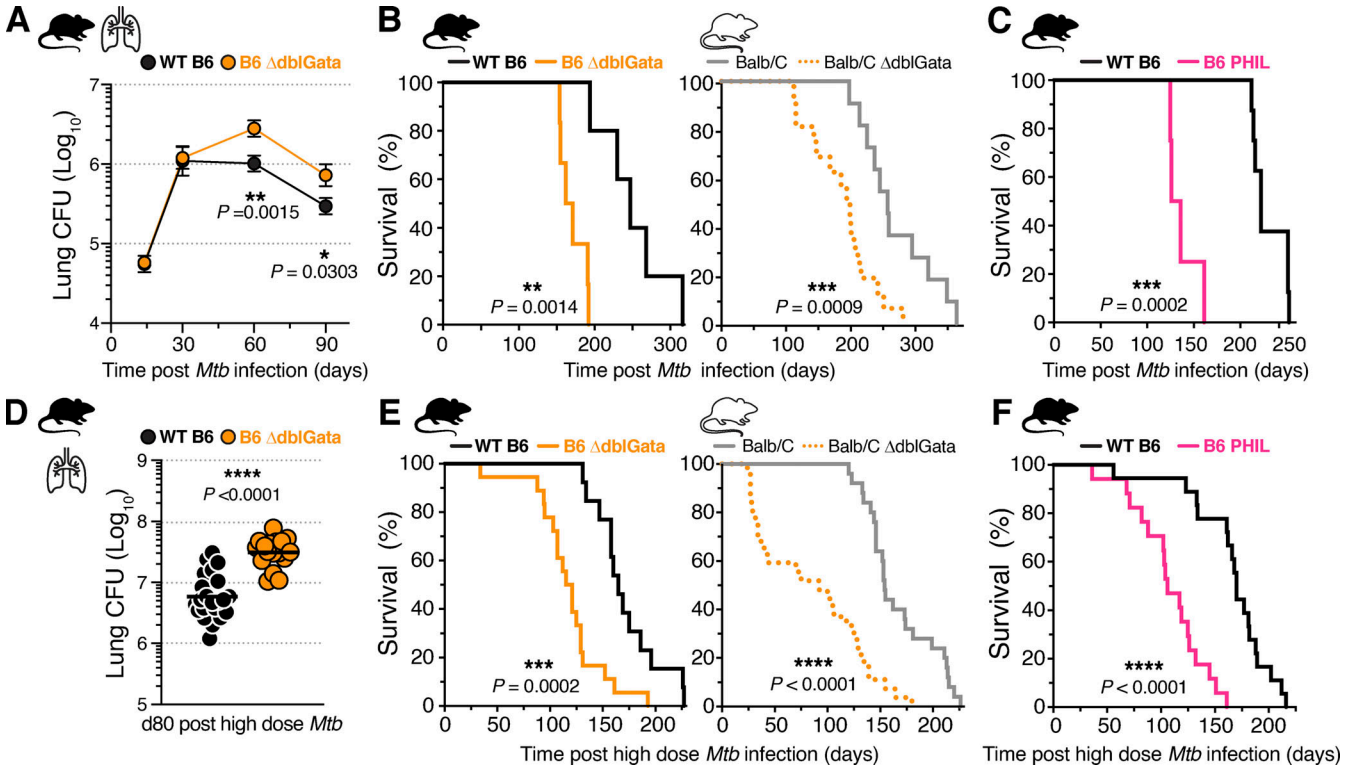

Figure 5. **Eosinophil deficiency in mice results in increased susceptibility to *Mtb* infection. (A)** CFU over time in lungs of WT B6 or B6 ΔdblGata mice infected with standard low-dose *Mtb* H37Rv (100–300 CFU; male and female, *n* = 11–21, two to three experiments per time point, Mann–Whitney test). **(B)** Survival of WT Balb/C or B6 or ΔdblGata infected with low-dose *Mtb* (100–300 CFU; male and female, *n* = 5–12, two to three experiments each, Mantel–Cox test). **(C)** Survival of WT B6 or PHIL mice after infection with 100–300 CFU *Mtb* (male and female, *n* = 4–8, two experiments each, Mantel–Cox test). **(D)** Lung CFU 80 d after high-dose (1,000–1,500 CFU) *Mtb* infection of WT B6 or B6 ΔdblGata mice (male and female, *n* = 11–21, three experiments, Mann-Whitney test). **(E)** Survival of WT Balb/C or B6 or ΔdblGata with 1,000–1,500 CFU *Mtb* infection (*n* = 13–27, three to four experiments each, Mantel–Cox test). **(F)** Survival of WT B6 or PHIL mice after infection with 1,000–1,500 CFU *Mtb* (male and female, *n* = 17–18, three experiments, Mantel–Cox test).

et al., 1997; Drake et al., 2018a; Drake et al., 2018b; Fryer and Wills-Karp, 1991; Kingham et al., 2002). Thus, our findings raise the possibility that eosinophils may be involved in pulmonary tissue–immune–nerve crosstalk during chronic infections.

Finally, to test whether eosinophils could influence the outcome of infection, we monitored pulmonary bacterial loads and survival in B6 ΔdblGata mice after *Mtb* infection. While lung bacterial loads were similar compared with WT mice for the first month, 2 mo after *Mtb* infection we consistently measured a significant 0.5–1-log increase in the lungs of B6 ΔdblGata mice (Fig. 5 A). Moreover, ΔdblGata mice on either B6 or Balb/C genetic backgrounds succumbed significantly earlier to *Mtb* infection (Fig. 5 B). To confirm these results in a second, independent genetic model of eosinophil deficiency, we infected transgenic B6 PHIL mice that express cytocidal diphtheria toxin A under the eosinophil-specific EPX promoter (Lee et al., 2004). Like B6 ΔdblGata mice, B6 PHIL mice succumbed significantly earlier than WT mice to *Mtb* infection (Fig. 5 C). When infected with a high dose of *Mtb*, both B6 ΔdblGata (Fig. 5 D) and PHIL (Fig. S3 N) mice displayed significantly increased lung bacterial loads at 2–3 mo and succumbed to *Mtb* infection–induced disease in an infectious dose-dependent manner (Fig. 5, E and F). Thus, the data from eosinophil-deficient mouse lines show that eosinophils play a functional role in optimal host resistance during *Mtb* infection.

To conclude, we found that eosinophils are recruited to *Mtb* lesions in humans, macaques, zebrafish, and mice. In human lung lesions, eosinophils were enriched compared with blood and found in TB granulomas. In NHP granulomas, eosinophils were present and functionally activated to degranulate. We observed diffuse granule protein staining in the necrotic cores of both human and NHP granulomas, indicative of eosinophil degranulation. In settings associated with tissue necrosis, *Mtb* can survive and propagate extracellularly (Basaraba and Hunter, 2017; Ernst, 2012), perhaps affording eosinophils the opportunity to access and kill extracellular *Mtb* via their characteristic degranulation and DNA trap formation. Moreover, purified human EPX has been reported to induce *Mtb* lysis in vitro (Borelli et al., 2003). Alternatively, granulocyte degranulation could facilitate necrotic core formation in granulomas. Thus, the described associations of eosinophils with TB granulomas in human and macaques do not allow for conclusions regarding protective or detrimental roles. In fact, it is likely that the biological function of eosinophils in host resistance to *Mtb* may be influenced by the stage and dose of infection, disease status, and granulomatous features, all factors that vary considerably between the broad host species examined in this study. Nevertheless, we establish here that eosinophils represent an unanticipated integral part of the lung granulocytic response to *Mtb* across species.

Importantly, our translational approach in mice uncovered an unexpected, yet functional role of eosinophils during murine *Mtb* infection. Using multiple eosinophil-deficient mouse lines, we show that eosinophils are required for optimal host survival and bacterial control. While the underlying protective mechanisms in mice are currently unclear, they could involve antibactericidal or immunoregulatory effector functions that directly or indirectly affect *Mtb* growth. However, we show here that neither phagocytosis nor direct infection with *Mtb* seem likely to be occurring at significant levels in eosinophils. Additional nondirect protective mechanisms are therefore likely and could involve immunomodulatory cell–cell interactions between eosinophils and *Mtb*-infected macrophages or other pulmonary immune cells, maintenance of lung barrier function, as well as disease tolerance. Such cell–cell interactions could involve production of lipid mediators, as identified in our GSEA, and type II cytokines. In fact, a recent study in zebrafish showed that noncanonical type II immune IL-4 and IL-13 signals played critical roles in mycobacterial granuloma formation and macrophage epithelialization (Cronan et al., 2021). Additionally, our transcriptional profiling revealed changes in neuronal-associated pathways, raising the intriguing possibility that eosinophils may also interact with nonimmune lung cells such as pulmonary neuroendocrine cells and airway sensory neurons. We therefore propose that eosinophil-mediated protection against *Mtb* likely includes multiple, nonmutually exclusive mechanisms, which remain to be experimentally explored further in mice and validated in interventional studies in NHPs.

Coinfection with parasitic helminths is common in areas with high TB incidence, and clinical studies have produced contradictory results on the effect of parasitic worm infections on TB outcomes (Babu and Nutman, 2016; Rafi et al., 2012). In some instances of improved clinical outcomes with TB–helminth coinfections (Abate et al., 2015; O'Shea et al., 2018; van Soelen et al., 2012), eosinophils may have contributed to improved outcomes. That said, increased susceptibility to bacterial infections has not been reported in clinical trials of eosinophil-depleting antibodies (Pavord et al., 2012; Rothenberg et al., 2008; Straumann et al., 2010), although longer-term data with examination of patients exposed to *Mtb* are needed, and it is possible that a protective effect of eosinophils is masked in highly heterogenous patient populations.

Taken together, our study represents a multispecies investigation of the eosinophil response to *Mtb*. Our data reveal that eosinophilic granulocytes, typically associated with type II inflammatory responses, represent an integral part of the granulocyte response to TB, a disease associated with type I immunity. Thus, our findings open up multiple new lines of investigation into the functional relevance of eosinophils during chronic bacterial lung infection and potential new targets for host-directed therapies for TB.

Materials and methods

Clinical study population in Shanghai, China

Human lung resection material was obtained at the Shanghai Public Health Clinical Center (SPHCC) between 2015 and 2019 following approval by the SPHCC Ethics Committee (#2015-S046-02 and #2019-S009-02). All patients provided written informed consent. Clinically indicated lung or pleural tissue resection surgery was performed at SPHCC as an adjunctive therapy for TB (L. Wang, Y. Song). Patients with HIV, other ongoing infections, or immunodeficiency conditions were excluded. Using sterile instruments, resected lung tissue samples from participants ID#1–4 were divided based on macroscopically apparent diverse tissue pathologies, and a minimum of triplicate samples for each pathological subtype was used for cell isolation and flow cytometric analysis. Participants ID#5–9 consented to ^{18}FDG PET/CT signal scanning 1–6 d before clinically indicated surgery to guide resection and minimize risk of postoperative complications, such as increasing bronchial stump and lung resection margin embedding. After resection, lung samples were further dissected, using sterile scissors, based on standardized uptake values (SUVs) into maximum-signal (PET high, SUV_{max} >5.0) and low-signal (PET low, similar to background SUV) pieces according to mapped ^{18}FDG PET/CT scanning results. Triplicate samples were generated for cell isolation and flow cytometric analysis for PET-high and -low regions from the same individuals. FACS studies were performed onsite by K.D. Mayer-Barber, Z. Hu, and K.-W. Wong, and samples were acquired on an LSRFortessa flow cytometer (BD Biosciences) and analyzed with FlowJo 10 software (FlowJo, LLC).

Participant ID#1

A 28-yr-old nonsmoker male, sputum smear and culture negative, received repeated ATT for 8 yr; drug resistance was not detected. Treatment before surgery: isoniazid, rifampicin (RIF), pyrazinamide, and ethambutol. Surgical indication: presence of cavities and irreversible TB progression with lung destruction. Postoperative pathological diagnosis: TB with large cavity with aspergilloma, extensive fibrotic lesions with a mixture of local cavities, granulomas, consolidations, and caseous necrosis. AFB was 4+ positive, and culture was positive for *Mtb*.

Participant ID#2

A 22-yr-old nonsmoker male; sputum smear and culture negative, drug resistance was not detected. Treatment before surgery: 4 mo treatment with isoniazid, RIF, pyrazinamide, ethambutol, and levofloxacin. Surgical indication: enlargement of pleural empyema. Postoperative pathological diagnosis: presence of inflammatory cells, fibrosis, coagulative necrosis, and caseous necrosis. Acid-fast smear staining was 2+ positive, and culture was positive for *Mtb*.

Participant ID#3

A 25-yr-old nonsmoker female; sputum smear and culture negative at time of surgery; sputum- and culture-confirmed diagnosis of PTB in both lungs in 2010 and repeated ATT over 6 yr; drug resistance to streptomycin, isoniazid, levofloxacin, and para-aminosalicylic acid was detected. Despite isoniazid, RIF, pyrazinamide, and ethambutol regimen treatment for 1 yr, reexamination of chest CT showed bilateral lesions were progressing and sputum culture was positive. Treatment before surgery: cycloserine, amikacin, linezolid, clofazimine, moxifloxacin, isoniazid, RIF, pyrazinamide, and ethambutol. Surgical

indication: the presence of multidrug resistance and cavities in the lower right lobe of the lung with complication of pneumothorax. Postoperative pathological diagnosis: tissue infiltration of inflammatory cells, epithelioid granuloma formation, caseous necrosis, and AFB (4+), which was not culture positive.

Participant ID#4

A 32-yr-old nonsmoker female; 5 yr of ATT, with extended drug resistance to streptomycin, isoniazid, RIF, and ofloxacin; sputum was 4+ smear positive and culture positive. Surgical indication: presence of extended drug resistance and consolidations and atelectasis in the lower right lobe of the lung. Postoperative pathological diagnosis: inflammatory cell infiltration, epithelioid granuloma formation, caseous necrosis, and AFB (2+), which was culture positive for *Mtb*.

Participant ID#5

A 20-yr-old nonsmoker female; drug resistance was not detected, positive sputum smear, anti-TB antibody and T-SPOT. Sputum smear was positive in July 2018. Treatment before surgery: 7-mo ATT with isoniazid, RIF, pyrazinamide, and ethambutol. Surgical indication: presence of tuberculous pleurisy–related tumor with increasing size over preceding 3 mo. Postoperative pathological diagnosis: inflammatory cell infiltration, epithelioid granuloma formation, and coagulation necrosis. Acid-fast smear staining was 4+.

Participant ID#6

A 38-yr-old male smoker (15-yr history); sputum smear and culture negative at time of surgery, no drug resistance 9 yr before surgery, patient received 1-yr ATT with isoniazid, RIF, pyrazinamide, and ethambutol after acid-fast smear positive test and CT showing improved TB lesions after treatment. Symptoms relapsed 3 yr before surgery, and he received ATT with isoniazid, RIF, pyrazinamide, ethambutol, levofloxacin, and azithromycin. Surgical indication: presence of repeated TB-related symptoms, including tuberculous pleuritis and cavities. Postoperative pathological diagnosis: epithelioid granuloma and coagulative necrosis. Tissue sample acid-fast smear staining was negative.

Participant ID#7

A 39-yr-old male smoker (20-yr history) with 5-yr history of TB had no drug resistance and negative sputum smear at time of surgery. He was previously treated with an isoniazid, RIF, pyrazinamide, and ethambutol regimen with positive sputum smear in the local hospital in August 2014 for 1 yr. TB recurred in June 2016, and ATT was repeated for 1 yr. In April 2018, the patient developed hemoptysis, and chest CT suggested left upper lobe TB with cavities. He received a third ATT. Treatment before surgery: 15-mo ATT with isoniazid, RIF, pyrazinamide, and ethambutol. TB antibody IgG was positive. Surgical indication: clinical diagnosis of tuberculous and persistent TB cavity despite ATT. Postoperative pathological diagnosis: tissue infiltration of inflammatory cells, granuloma formation, coagulative necrosis, calcification, focal pulmonary hemorrhage, and local fungal infection. Acid-fast smear staining was negative, and periodic acid–Schiff (PAS) staining was positive.

Participant ID#8

In a 57-yr-old male nonsmoker, sputum smear and anti-TB antibody were positive, and RIF resistance was detected by GeneXpert (GXPT; Cepheid). Treatment before surgery: 1-mo ATT with RIF, pyrazinamide, ethambutol, isoniazid, and levofloxacin (stopped due to cutaneous pruritus) and 1-mo treatment with rifapentine. Surgical indication: presence of lung cavity. Postoperative pathological diagnosis: inflammatory cell infiltration, epithelioid granuloma formation, and coagulation necrosis. Fluid from the postoperative lesion was acid-fast smear 3+, GXPT positive for *Mtb*, and RIF sensitive.

Participant ID#9

A 23-yr-old female nonsmoker was diagnosed with PTB in 2016 (positive sputum smear). ATT with isoniazid, RIF, pyrazinamide, and ethambutol was discontinued after 6 mo; fatigue, night sweats, and large pleural effusion occurred in 2018, and the sputum smear was positive again. No drug resistance was found prior to ATT. Treatment before surgery: 10-mo ATT with isoniazid, RIF, ethambutol, levofloxacin, bicyclol, and amikacin. Surgical indication: clinical diagnosis of tuberculous hydrothorax and destructive pneumophthisis. Postoperative pathological diagnosis: tissue infiltration of inflammatory cells, epithelioid granuloma formation, fibrosis, and coagulative necrosis. GXPT test on intraoperative endocrine-resected tissue revealed RIF-sensitive *Mtb* complex.

Clinical study populations in Cape Town, South Africa

For eosinophil studies from Cape Town, South Africa, participants were recruited from the Site B Community Health Centre in Khayelitsha between March 2017 and December 2018. Some study participants are described elsewhere (Du Bruyn et al., 2021) and in Table 1. Briefly, all participants were HIV-uninfected adults (age ≥ 18 yr) who provided written informed consent. The study was approved by the University of Cape Town Human Research Ethics Committee (HREC 050/2015) and was conducted under Diagnostic Microbiology and Infectious Disease protocol no. 15-0047. Those in the active TB group (PTB, $n = 48$) all tested sputum GXPT (Cepheid) *Mtb*/RIF and/or sputum *Mtb* liquid culture positive. All active TB cases were drug sensitive and had received no more than one dose of ATT at the time of baseline blood sampling. Participants in the LTBI group ($n = 77$) were all asymptomatic with a positive IFN-γ release assay (IGRA; QuantiFERON TB Gold In-Tube), tested sputum GXPT *Mtb*/RIF negative, and had no clinical or radiographical evidence of active TB. Similarly, participants in the healthy control (HC) group ($n = 20$) were all asymptomatic without a history of previous TB, tested sputum GXPT *Mtb*/RIF negative, had no clinical or radiographical evidence of active TB, and tested IGRA negative. Sputum GXPT *Mtb*/RIF and differential full blood count were performed by the South African National Health Laboratory Services.

Clinical study population in Zhengzhou, China

HIV-uninfected individuals with symptoms indicative of active TB who were administered <2 wk of ATT were enrolled in a natural history study to assess response to chemotherapy

Table 1. **Cape Town, South Africa, patient characteristics**

Characteristic	HC; IGRA⁻	LTBI; IGRA⁺	Active PTB; sputum GXPT⁺
n (HIV negative)	20	77	48
Average age (yr)	38	33	37
Sex (female/male)	12/8	39/38	13/35

(NCT01071603) conducted at the Henan Chest Hospital in Zhengzhou, China, from 2010 to 2012. For detailed descriptions of the clinical cohort, see Mayer-Barber et al. (2014) and others (Trauner et al., 2017; Vinhaes et al., 2019).

Clinical study population in London, UK

The clinical study population of the TB patients in London, UK, who were retrospectively identified by database and case note review at the King's College Hospital and Newham University Hospital Trust, has been described in detail in Lowe et al. (2013).

Clinical autopsy cohort from Rome, Italy

The autopsy cohort from the National Institute for Infectious Diseases, "Lazzaro Spallanzani," in Rome, Italy, included neutral-buffered, formalin-fixed paraffin-embedded autopsy lung tissue samples from patients with histologically, histochemically, or PCR-proven confirmed PTB as previously described in Blauenfeldt et al. (2018).

Clinical study population in Bethesda, MD

For WB flow cytometry or in vitro experiments on eosinophils, HCs from the National Institutes of Health (NIH) in Bethesda, MD, were recruited through an institutional review board–approved clinical protocol to obtain normal blood samples (NCT00001846). All participants gave written informed consent.

Rhesus macaques

13 healthy >2-yr-old rhesus macaques (male and female, tuberculin skin test negative) were received from the National Institute of Allergy and Infectious Diseases (NIAID) breeding colony on Morgan Island. Animals were housed in NHP biocontainment racks and maintained in accordance with the Animal Welfare Act; Guide for the Care and Use of Laboratory Animals; and all applicable regulations, standards, and policies in a fully American Association for Accreditation of Laboratory Animal Care International–accredited Animal Biosafety Level 3 vivarium. All procedures were performed using appropriate anesthetics as listed in the NIAID Division of Intramural Research Animal Care and Use Committee–approved animal study proposal LPD25E. Euthanasia methods were consistent with the American Veterinary Medical Association Guidelines on Euthanasia and end point criteria listed in the NIAID Division of Intramural Research Animal Care and Use Committee–approved animal study proposal.

Mtb infections of rhesus macaques

Rhesus macaques from two independent infections provided tissues for this study (Fig. S2 B), and animals DF4A, 0DH, DF8B, and DFNO have previously been reported in another study (Sallin et al., 2018). Individual macaques were infected with 30–50 CFU of either H37Rv or mCherry-expressing Erdman strain of *Mtb*. For infections, animals were anesthetized, and 2 ml of *Mtb*-containing saline was instilled bronchoscopically into the right lower lung lobe. Delivered infection doses were confirmed by plating aliquots of instillation solution onto 7H11 agar plates. Colony counts were determined after 21 d.

Mice

B6 mice were purchased from Taconic Farms. B6 PHIL mice (Lee et al., 2004) were obtained from Elizabeth Jacobsen (Mayo Clinic, Phoenix, AZ). B6 ΔdblGata (JAX 33551, B6.129S1(C)-Gata1tm6Sho/LvtzJ) mice were provided by Helene Rosenberg (NIAID, Bethesda, MD). ΔdblGata (JAX 5653, C.129S1(B6)-Gata1tm6Sho/J) on the BALB/cJ background mice were purchased from The Jackson Laboratory. Both male and female mice, 8–24 wk old at the onset of experiments, were used, and experimental groups in individual experiments were age and sex matched. All animals were bred and maintained in an American Association for Accreditation of Laboratory Animal Care–accredited ABSL2 or ABSL3 facility at NIH, and experiments were performed in compliance with an animal study proposal approved by the NIAID Animal Care and Use Committee (protocol LCIM17E).

Mtb infections of mice

For aerosol infection of mice with H37Rv strains of *Mtb*, animals were placed in a whole-body inhalation exposure system (Glas-Col) and exposed to aerosolized *Mtb*. Delivery doses (100–300 CFU for standard low dose, 1,000–1,500 CFU for high dose) were confirmed by measuring lung bacterial loads at 2–24 h after exposure in control mice. Bacterial loads were measured in tissue homogenates obtained via digestion and dissociation using gentleMACS (Miltenyi Biotec) or mechanical homogenization using Precellys Evolution (Bertin Instruments). Lung homogenates were serially diluted in PBS/Tween-20 and cultured on Middlebrook 7H11 agar plates supplemented with oleic acid–albumin–dextrose catalase (Difco Laboratories). Colony counts were determined after 21 d. H37Rv-mCherry was provided by Kevin Urdahl (Seattle Children's, Seattle, WA; Cohen et al., 2018).

M. marinum infection and paraffin embedding of zebrafish

All zebrafish husbandry and experiments were approved by the Duke University Animal Care and Use Committee (protocol A122-17-05). Single-cell aliquots of cerulean-expressing *M. marinum* were made according to the method of Takaki et al. (2013). Zebrafish were anesthetized with 0.016% tricaine and

infected with *M. marinum*–expressing cerulean fluorescent protein at a dose of 400 fluorescent bacteria/animal by intraperitoneal injection. Zebrafish were maintained in spawning tanks with daily water changes. At 2 wk after infection, zebrafish were euthanized by tricaine overdose and the head and tail removed with a scalpel. A small incision was made in the belly, and the zebrafish were fixed for 2 d in 4% paraformaldehyde. The animals were subsequently processed and paraffin embedded by the Duke Research Immunohistology Laboratory.

Histopathology

Tissue samples were fixed with 4% paraformaldehyde, paraffin embedded, sectioned, and stained with either H&E, the Ziehl–Nielsen histochemical method to visualize acid-fast mycobacteria, anti-EPX for the immunohistochemical identification of eosinophils, or PAS for necrosis. Eosinophils were identified via light microscopy using an Olympus BX51 microscope (magnifications of 4×, 10×, 20×, or 40×) and photomicrographs taken using an Olympus DP73 camera. The distribution of eosinophil staining was assessed microscopically using indicated scales; all histological analyses were scored in a blinded manner by a board-certified veterinary pathologist.

Confocal microscopy of rhesus macaque granulomas

Excised granulomas from Erdman-mCherry–fluorescent *Mtb*-infected rhesus macaques were fixed overnight in 4% paraformaldehyde and subsequently embedded in optimal cutting temperature compound (Thermo Fisher Scientific) and stored at −80°C . Cryostat-cut sections (7 µm) were placed onto microscope slides (Thermo Fisher Scientific) and blocked with 10% FCS in PBS and incubated with anti-laminin-AF647 and anti-human EPX AF488 for 1 h at 37°C in a humidified chamber. Afterward, the slides were washed in PBS for 10 min and mounted with ProLong Gold Antifade Mountant (Thermo Fisher Scientific). The samples were analyzed with a Leica SP8 confocal laser fluorescence microscope and Imaris software (Bitplane).

RNA extraction and sequencing

For RNA extraction, dedicated lung lobes were placed in RNAlater (Invitrogen) and stored at −80°C. RNAlater-stabilized lung lobes were thawed at RT for 20 min, then homogenized in RLT Plus buffer with β-mercaptoethanol (QIAGEN). Total RNA was then isolated from the RLT-homogenized cells using the RNeasy Plus Mini Kit (QIAGEN). RNA quantification, qualification, as well as library preparation and transcriptome sequencing were performed by Novogene Corporation. Briefly, RNA degradation and contamination was monitored on 1% agarose gels, and RNA purity was checked using the NanoPhotometer Spectrophotometer (IMPLEN). RNA integrity and quantitation were assessed using the RNA Nano 6000 Assay Kit of the Bioanalyzer 2100 system (Agilent Technologies). A total amount of 1 µg RNA per sample was used as input material for the RNA sample preparations. Sequencing libraries were generated using NEBNext Ultra RNA Library Prep Kit for Illumina (New England Biolabs) following the manufacturer's recommendations, and index codes were added to attribute sequences to each sample. Briefly, mRNA was purified from total RNA using poly-T oligo–attached magnetic beads. Fragmentation was performed using divalent cations under elevated temperature in NEBNext First Strand Synthesis Reaction Buffer (5×). First strand cDNA was synthesized using random hexamer primer and M-MuLV Reverse Transcriptase (RNase H−). Second strand cDNA synthesis was subsequently performed using DNA Polymerase I and RNase H. Remaining overhangs were converted into blunt ends via exonuclease/polymerase activities. After adenylation of 3′ ends of DNA fragments, NEBNext Adaptor with hairpin loop structure were ligated to prepare for hybridization. To select cDNA fragments of preferentially 150∼200 bp in length, the library fragments were purified with AMPure XP system (Beckman Coulter). Then 3-µl USER Enzyme (New England Biolabs) was used with size-selected, adaptor–ligated cDNA at 37°C for 15 min followed by 5 min at 95°C before PCR. PCR then was performed with Phusion High-Fidelity DNA Polymerase and Universal and Index Primers. Finally, PCR products were purified (AMPure XP system), and library quality was assessed using the Agilent Bioanalyzer 2100 system. The clustering of the index-coded samples was performed on a cBot Cluster Generation System using PE Cluster Kit cBot-HS (Illumina) according to the manufacturer's instructions. After cluster generation, the library preparations were sequenced on an Illumina NovaSeq 6000 platform, and paired-end 150-bp reads were generated. The entire gene expression dataset is available in Gene Expression Omnibus under accession no. GSE165871.

Transcriptional analysis

For all samples, low-quality bases were removed and adapters trimmed using Trimmomatic v0.32 (Bolger et al., 2014). After the quality check, sequences were aligned to the *Mus musculus* genome (GRCm38.p6 version 67) with STAR 2.7.0 (Dobin et al., 2013). After mapping, the output was converted to count tables with the tximport package (Soneson et al., 2015) from R 4.0.2. The stratification was performed as follows: d0 WT B6 group was composed of five samples: d0WT1–d0WT5, d0 ΔdblGata group (d0Gata1–4), d90 WT B6 group (d90WT1–4), and d90 ΔdblGata group (d90Gata1–5). Count gene expression matrix was examined by the DESeq2 package (Love et al., 2014) from R 4.0.2 to identify DEGs using the following the comparisons: d90 ΔdblGata versus d90 WT B6, d0 ΔdblGata versus d0 WT B6, d90 ΔdblGata versus d0 WT B6, and d90 WT B6 versus d0 WT B6. Changes in gene expression levels were considered significant when statistical test values (false discovery rate [FDR]–adjusted P value) were <0.05 and the fold change/difference higher than ±1.4. Candidate DEGs were visualized by volcano plots and Venn diagrams with the EnhancedVolcano and VennDiagram packages from R 4.0.2. The obtained DEGs were scanned by Reactome (Yu and He, 2016) and Kyoto Encyclopedia of Genes and Genomes (http://www.genome.jp/kegg/) pathway database using the compareCluster package (Yu et al., 2012) from R 4.0.2. The gene list of IFN-inducible (type I) and IFN-γ–inducible (type II) lung modules were retrieved from Singhania et al. (2019). The sample clustering and classification were assessed using heatmaps and applied in the variance-stabilizing transformation gene expression values.

Cell isolations for flow cytometry: Peripheral blood

Rhesus macaque and human blood samples were collected in EDTA tubes, and WB was used for flow cytometry. Briefly, antibody cocktails were directly added to 200 µl of WB and stained at 37°C for 20 min, after which samples were washed twice in 4 ml 1% FCS/PBS. Fixable live/dead cell stain (Molecular Probes; Invitrogen) was used according to the manufacturer's protocol. Pellets were then fixed and permeabilized with the eBioscience Foxp3 Transcription Factor Staining Buffer Kit (Life Technologies) for at least 1 h followed by intracellular antigen staining for 30 min at 4°C. Cells were washed and samples acquired on a FACSymphony (BD Biosciences) at NIH or an LSRFortessa (BD Biosciences) at SPHCC. FACS data were analyzed using FlowJo 10 (FlowJo, LLC).

Cell isolations for flow cytometry: BAL and granulomas from rhesus macaques

Rhesus macaque BAL samples were passed through a 100-µm cell strainer, pelleted, and counted for analysis. Granulomas were individually resected from the lungs, and samples used for flow cytometry analysis were pushed through a 100-µm cell strainer. Aliquots from all samples were serially diluted and plated on 7H11 agar plates for CFU quantification. Alternatively, resected granulomas were fixed in 4% paraformaldehyde for later paraffin embedding. Samples were stained with surface antibody cocktails for 20 min at 4°C followed by fixable live/dead cell stain (Molecular Probes; Invitrogen). Cells were then fixed and permeabilized (eBioscience Transcription Factor Staining Buffer Kit) for at least 1 h followed by intracellular antigen staining for 30 min at 4°C. Cells were washed and samples acquired on a FACSymphony (BD Biosciences) at NIH. FACS data were analyzed using FlowJo 10 (FlowJo, LLC).

Cell isolations for flow cytometry: Human and murine lung tissue

Mice were i.v. injected 3 min before euthanasia with 5 µg/mouse APC- or BV711-labeled CD45 (30-F11) as previously reported (Anderson et al., 2014). Lungs from infected mice were digested using a lung cell isolation buffer and dissociated via gentleMACS (Miltenyi Biotec) according to the manufacturer's instructions. Digested lung was fully dispersed by passage through a 100-µm cell strainer, and an aliquot was removed for bacterial load measurements. Cells were then washed and purified using a 37% Percoll step. Samples were stained with surface antibody cocktails for 20 min at 4°C followed by fixable live/dead cell stain (Molecular Probes; Invitrogen). Cells were then fixed and permeabilized (eBioscience Transcription Factor Staining Buffer Kit) for at least 1 h followed by intracellular antigen staining for 30 min at 4°C. Cells were washed and samples acquired on a FACSymphony (BD Biosciences) at NIH. FACS data were analyzed using FlowJo 10 (FlowJo, LLC).

The surgically resected human lung tissue samples were weighed and manually aliquoted into replicates using sterile scissors inside a sterile 50-ml tube. Aliquots were transferred into Trizol for RNA isolation or subjected to single-cell isolation. Briefly, sample replicates for single-cell isolation were digested with 100 U/ml of collagenase IV (Sigma) and 50 U/ml of Benzonase (Sigma) in 8 ml of incomplete RPMI-1640 medium (without FBS) for 45 min at 37°C in a shaker. Cells were then filtered through 100-µm cell strainers (Miltenyi Biotec), and the remainder of tissue pieces were gently squashed by a syringe and washed with 4 ml ice-cold PBS containing 50% FBS to stop digestion. Next, the cell suspension was centrifuged and subjected to Debris Removal Solution (Miltenyi Biotec) according to the manufacturer's protocol. Samples were stained with surface antibody cocktails for 20 min at 4°C followed by fixable live/dead cell stain (Molecular Probes; Invitrogen). Cells were then fixed and permeabilized (eBioscience Transcription Factor Staining Buffer Kit) for at least 1 h followed by intracellular antigen staining for 30 min at 4°C. Cells were washed and samples acquired on an LSRFortessa (BD Biosciences) at SPHCC. FACS data were analyzed using FlowJo 10 (FlowJo, LLC).

Flow cytometry reagents

Fluorochrome-labeled antibodies against mouse, human, or rhesus macaque antigens used for flow cytometric analysis are as follows: I-A/I-E (clone M5/114.15.2), Ly6G (1A8), CD11c (HL3 and N418), CD45.2 (104), TCRb (H57-597), NK1.1 (PK136), CD11b (M1/70), CD45 (30-F11), CD68 (FA-11), Ly6C (AL-21 and HK1.4), Siglec-F (E50-2440), CD193 (J073E5), Arg1 (A1exF5), NOS2 (CXNFT), CD4 (L3T4), CD8a (53-6.7), Foxp3 (FJK-16s), CD193 (5E8.4), EPX (AHE-1), CD62L (MEL-14), CD14 (M5E2), CD11c (3.9), CD45 (D058-1283), CD66abce (TET2), CD15 (HI98), CD68 (Y1/82A), HLA-DR (L243), CD16 (3G8), CD45 (2D1), CD193 (83101), CD66b (G10F5), CD62L (REG-56), CD206 (15–2.2), CD123 (6H6), and Siglec-8 (7C9). ESAT-$6_{1–17}$ or TB10.$4_{4–11}$ tetramers were produced by the NIAID tetramer core facility (Emory University, Atlanta, GA).

Statistical analyses

The statistical significance of differences between data groups was calculated using GraphPad Prism 8. The Mann–Whitney test and Wilcoxon matched pairs test (PET low versus high, otherwise paired samples) were used for comparison of group means, log-rank Mantel–Cox test was used for survival data, and Spearman correlation test was used unless otherwise indicated in the figures or figure legends.

Online supplemental material

Fig. S1 shows additional clinical data and study designs. Fig. S2 shows human and NHP granuloma structures with eosinophil distribution and EPX staining specificity. Fig. S3 shows depletion efficiency in eosinophil-deficient mouse strains after *Mtb* infection and additional transcriptional and immunological parameters assessed in ΔdblGata and increased bacterial loads in B6 PHIL mice. Table S1 lists RNA sequencing analysis results of DEGs, modules, and GSEA.

Acknowledgments

We thank the clinical study participants and medical staff at the Khayelitsha Site B Community Health Centre in Cape Town, the SPHCC affiliated with Fudan University in Shanghai, and the Henan Chest Hospital in Zhengzhou. We also thank Drs. Y. Belkaid, A. O'Garra, S.P. Babu, M. Lionakis, and A. Sher for data discussions

and feedback on the manuscript. We are grateful to Ray Y. Chen for assistance with clinical protocol, all Tuberculosis Imaging Program members, and the staff of the NIAID ABSL2 and ABSL3 facilities.

This work was supported in part by the Division of Intramural Research, National Institute of Allergy and Infectious Diseases (K.D. Mayer-Barber, D.L. Barber, C.E. Barry III, L.E. Via) and the National Natural Science Foundation of China (grant no. 81770010 to K.-W. Wong). R.J. Wilkinson is supported by the National Institutes of Health (grant no. U01AI115940), Wellcome Trust (grant nos. 104803 and 203135), and Cancer Research UK, UK Research and Innovation, and Wellcome Trust (FC0010218). B.B. Andrade is supported by the National Council for Scientific and Technological Development (senior fellowship) and by the Intramural Research Program of the Oswaldo Cruz Foundation, Brazil. This research was funded in whole or in part by Wellcome Trust. For the purpose of Open Access, the author has applied a CC-BY public copyright license to any Author Accepted Manuscript (AAM) version arising from this submission.

Author contributions: Conceptualization: Y. Song, A.D. Klion, K.-W. Wong, and K.D. Mayer-Barber. Methodology: A.C. Bohrer, E. Castro, Z. Hu, L. Wang, Tuberculosis Imaging Program, Y. Song, K.-W. Wong, and K.D. Mayer-Barber. Investigation: A.C. Bohrer, E. Castro, Z. Hu, C.E. Tocheny, M. Assmann, C. Nelson, P.J. Baker, H. Ma, L. Wang, W. Zilu, S. Sakai, E. du Bruyn, C. Riou, K.D. Kauffman, Tuberculosis Imaging Program, I.N. Moore, D.M. Lowe, K.-W. Wong, and K.D. Mayer-Barber. Resources: A.R. Martineau, D.M. Lowe, L. Wang, Tuberculosis Imaging Program, F. Del Nonno, L. Petrone, D. Goletti, M.R. Cronan, R.J. Wilkinson, C.E. Barry III, L.E. Via, D.L. Barber, Y. Song, K.-W. Wong, and K.D. Mayer-Barber. Data analysis and curation: A.C. Bohrer, E. Castro, Z. Hu, E. du Bruyn, C. Riou, C.E. Tocheny, M. Assmann, Tuberculosis Imaging Program, H. Ma, A.T.L. Queiroz, B.B. Andrade, and K.D. Mayer-Barber. Writing-original draft: K.D. Mayer-Barber. Writing-review and editing: all authors. Visualization: A.C. Bohrer, A.T.L. Queiroz, and K.D. Mayer-Barber. Supervision: B.B. Andrade, D.L. Barber, L.E. Via, R.J. Wilkinson, Y. Song, K.-W. Wong, and K.D. Mayer-Barber. Funding acquisition: B.B. Andrade, D.L. Barber, L.E. Via, K.-W. Wong, and K.D. Mayer-Barber.

Disclosures: D.M. Lowe reported personal fees from Merck, non-financial support from CSL Behring, and non-financial support from Fujifilm Chemical Co. outside the submitted work. No other disclosures were reported.

Submitted: 24 February 2021
Revised: 16 May 2021
Accepted: 13 July 2021

References

Abate, E., M. Belayneh, J. Idh, E. Diro, D. Elias, S. Britton, A. Aseffa, O. Stendahl, and T. Schön. 2015. Asymptomatic helminth infection in active tuberculosis is associated with increased regulatory and Th-2 responses and a lower sputum smear positivity. *PLoS Negl. Trop. Dis.* 9: e0003994. https://doi.org/10.1371/journal.pntd.0003994

Acharya, K.R., and S.J. Ackerman. 2014. Eosinophil granule proteins: Form and function. *J. Biol. Chem.* 289:17406–17415. https://doi.org/10.1074/jbc.R113.546218

Anderson, K.G., K. Mayer-Barber, H. Sung, L. Beura, B.R. James, J.J. Taylor, L. Qunaj, T.S. Griffith, V. Vezys, D.L. Barber, and D. Masopust. 2014. Intravascular staining for discrimination of vascular and tissue leukocytes. *Nat. Protoc.* 9:209–222. https://doi.org/10.1038/nprot.2014.005

Arnold, I.C., M. Artola-Borán, P. Tallón de Lara, A. Kyburz, C. Taube, K. Ottemann, M. van den Broek, S. Yousefi, H.U. Simon, and A. Müller. 2018. Eosinophils suppress Th1 responses and restrict bacterially induced gastrointestinal inflammation. *J. Exp. Med.* 215:2055–2072. https://doi.org/10.1084/jem.20172049

Babu, S., and T.B. Nutman. 2016. Helminth-tuberculosis co-infection: An immunologic perspective. *Trends Immunol.* 37:597–607. https://doi.org/10.1016/j.it.2016.07.005

Basaraba, R.J., and R.L. Hunter. 2017. Pathology of Tuberculosis: How the Pathology of Human Tuberculosis Informs and Directs Animal Models. *Microbiol. Spectr.* 5:TBTB2-0029-2016. https://doi.org/10.1128/microbiolspec.TBTB2-0029-2016

Blauenfeldt, T., L. Petrone, F. Del Nonno, A. Baiocchini, L. Falasca, T. Chiacchio, V. Bondet, V. Vanini, F. Palmieri, G. Galluccio, et al. 2018. Interplay of DDP4 and IP-10 as a potential mechanism for cell recruitment to tuberculosis lesions. *Front. Immunol.* 9:1456. https://doi.org/10.3389/fimmu.2018.01456

Bolger, A.M., M. Lohse, and B. Usadel. 2014. Trimmomatic: A flexible trimmer for Illumina sequence data. *Bioinformatics.* 30:2114–2120. https://doi.org/10.1093/bioinformatics/btu170

Borelli, V., F. Vita, S. Shankar, M.R. Soranzo, E. Banfi, G. Scialino, C. Brochetta, and G. Zabucchi. 2003. Human eosinophil peroxidase induces surface alteration, killing, and lysis of Mycobacterium tuberculosis. *Infect. Immun.* 71:605–613. https://doi.org/10.1128/IAI.71.2.605-613.2003

Bozkurt, T.E. 2019. Endocannabinoid system in the airways. *Molecules.* 24: 24244626. https://doi.org/10.3390/molecules24244626

Chesné, J., V. Cardoso, and H. Veiga-Fernandes. 2019. Neuro-immune regulation of mucosal physiology. *Mucosal Immunol.* 12:10–20. https://doi.org/10.1038/s41385-018-0063-y

Cohen, S.B., B.H. Gern, J.L. Delahaye, K.N. Adams, C.R. Plumlee, J.K. Winkler, D.R. Sherman, M.Y. Gerner, and K.B. Urdahl. 2018. Alveolar macrophages provide an early mycobacterium tuberculosis niche and initiate dissemination. *Cell Host Microbe.* 24:439–446.e4. https://doi.org/10.1016/j.chom.2018.08.001

Cooper, A.M., D.K. Dalton, T.A. Stewart, J.P. Griffin, D.G. Russell, and I.M. Orme. 1993. Disseminated tuberculosis in interferon gamma gene-disrupted mice. *J. Exp. Med.* 178:2243–2247. https://doi.org/10.1084/jem.178.6.2243

Costello, R.W., B.H. Schofield, G.M. Kephart, G.J. Gleich, D.B. Jacoby, and A.D. Fryer. 1997. Localization of eosinophils to airway nerves and effect on neuronal M2 muscarinic receptor function. *Am. J. Physiol.* 273:L93–L103. https://doi.org/10.1152/ajplung.1997.273.1.L93

Cronan, M.R., E.J. Hughes, W.J. Brewer, G. Viswanathan, E.G. Hunt, B. Singh, S. Mehra, S.H. Oehlers, S.G. Gregory, D. Kaushal, and D.M. Tobin. 2021. A non-canonical type 2 immune response coordinates tuberculous granuloma formation and epithelialization. *Cell.* 184:1757–1774.e14. https://doi.org/10.1016/j.cell.2021.02.046

Dobin, A., C.A. Davis, F. Schlesinger, J. Drenkow, C. Zaleski, S. Jha, P. Batut, M. Chaisson, and T.R. Gingeras. 2013. STAR: Ultrafast universal RNA-seq aligner. *Bioinformatics.* 29:15–21. https://doi.org/10.1093/bioinformatics/bts635

Drake, M.G., K.M. Lebold, Q.R. Roth-Carter, A.B. Pincus, E.D. Blum, B.J. Proskocil, D.B. Jacoby, A.D. Fryer, and Z. Nie. 2018a. Eosinophil and airway nerve interactions in asthma. *J. Leukoc. Biol.* 104:61–67. https://doi.org/10.1002/JLB.3MR1117-426R

Drake, M.G., G.D. Scott, E.D. Blum, K.M. Lebold, Z. Nie, J.J. Lee, A.D. Fryer, R.W. Costello, and D.B. Jacoby. 2018b. Eosinophils increase airway sensory nerve density in mice and in human asthma. *Sci. Transl. Med.* 10:aar8477. https://doi.org/10.1126/scitranslmed.aar8477

Du Bruyn, E., S. Ruzive, C.S. Lindestam Arlehamn, A. Sette, A. Sher, D.L. Barber, R.J. Wilkinson, and C. Riou. 2021. Mycobacterium tuberculosis-specific CD4 T cells expressing CD153 inversely associate with bacterial load and disease severity in human tuberculosis. *Mucosal Immunol.* 14: 491–499. https://doi.org/10.1038/s41385-020-0322-6

Ernst, J.D. 2012. The immunological life cycle of tuberculosis. *Nat. Rev. Immunol.* 12:581–591. https://doi.org/10.1038/nri3259

Flynn, J.L., and J.D. Ernst. 2000. Immune responses in tuberculosis. *Curr. Opin. Immunol.* 12:432–436. https://doi.org/10.1016/S0952-7915(00)00116-3

Flynn, J.L., J. Chan, K.J. Triebold, D.K. Dalton, T.A. Stewart, and B.R. Bloom. 1993. An essential role for interferon gamma in resistance to *Mycobacterium tuberculosis* infection. *J. Exp. Med.* 178:2249–2254. https://doi.org/10.1084/jem.178.6.2249

Flynn, J.L., H.P. Gideon, J.T. Mattila, and P.L. Lin. 2015. Immunology studies in non-human primate models of tuberculosis. *Immunol. Rev.* 264:60–73. https://doi.org/10.1111/imr.12258

Fryer, A.D., and M. Wills-Karp. 1991. Dysfunction of M2-muscarinic receptors in pulmonary parasympathetic nerves after antigen challenge. *J Appl Physiol (1985)*. 71:2255–2261. https://doi.org/10.1152/jappl.1991.71.6.2255

Huang, L., E.V. Nazarova, S. Tan, Y. Liu, and D.G. Russell. 2018. Growth of *Mycobacterium tuberculosis* in vivo segregates with host macrophage metabolism and ontogeny. *J. Exp. Med.* 215:1135–1152. https://doi.org/10.1084/jem.20172020

Kingham, P.J., W.G. McLean, D.A. Sawatzky, M.T. Walsh, and R.W. Costello. 2002. Adhesion-dependent interactions between eosinophils and cholinergic nerves. *Am. J. Physiol. Lung Cell. Mol. Physiol.* 282:L1229–L1238. https://doi.org/10.1152/ajplung.00278.2001

Kirman, J., Z. Zakaria, K. McCoy, B. Delahunt, and G. Le Gros. 2000. Role of eosinophils in the pathogenesis of *Mycobacterium bovis* BCG infection in gamma interferon receptor-deficient mice. *Infect. Immun.* 68:2976–2978. https://doi.org/10.1128/IAI.68.5.2976-2978.2000

Klion, A.D., and T.B. Nutman. 2004. The role of eosinophils in host defense against helminth parasites. *J. Allergy Clin. Immunol.* 113:30–37. https://doi.org/10.1016/j.jaci.2003.10.050

Klion, A.D., S.J. Ackerman, and B.S. Bochner. 2020. Contributions of eosinophils to human health and disease. *Annu. Rev. Pathol.* 15:179–209. https://doi.org/10.1146/annurev-pathmechdis-012419-032756

Krishack, P.A., T.J. Louviere, T.S. Decker, T.G. Kuzel, J.A. Greenberg, D.F. Camacho, C.L. Hrusch, A.I. Sperling, and P.A. Verhoef. 2019. Protection against Staphylococcus aureus bacteremia-induced mortality depends on ILC2s and eosinophils. *JCI Insight.* 4:124168. https://doi.org/10.1172/jci.insight.124168

Lasco, T.M., O.C. Turner, L. Cassone, I. Sugawara, H. Yamada, D.N. McMurray, and I.M. Orme. 2004. Rapid accumulation of eosinophils in lung lesions in guinea pigs infected with Mycobacterium tuberculosis. *Infect. Immun.* 72:1147–1149. https://doi.org/10.1128/IAI.72.2.1147-1149.2004

Lee, J.J., D. Dimina, M.P. Macias, S.I. Ochkur, M.P. McGarry, K.R. O'Neill, C. Protheroe, R. Pero, T. Nguyen, S.A. Cormier, et al. 2004. Defining a link with asthma in mice congenitally deficient in eosinophils. *Science.* 305:1773–1776. https://doi.org/10.1126/science.1099472

Lee, J.J., E.A. Jacobsen, M.P. McGarry, R.P. Schleimer, and N.A. Lee. 2010. Eosinophils in health and disease: The LIAR hypothesis. *Clin. Exp. Allergy.* 40:563–575. https://doi.org/10.1111/j.1365-2222.2010.03484.x

Lee, J., S. Boyce, J. Powers, C. Baer, C.M. Sassetti, and S.M. Behar. 2020. CD11cHi monocyte-derived macrophages are a major cellular compartment infected by Mycobacterium tuberculosis. *PLoS Pathog.* 16:e1008621. https://doi.org/10.1371/journal.ppat.1008621

Lilly, L.M., M. Scopel, M.P. Nelson, A.R. Burg, C.W. Dunaway, and C. Steele. 2014. Eosinophil deficiency compromises lung defense against Aspergillus fumigatus. *Infect. Immun.* 82:1315–1325. https://doi.org/10.1128/IAI.01172-13

Linch, S.N., A.M. Kelly, E.T. Danielson, R. Pero, J.J. Lee, and J.A. Gold. 2009. Mouse eosinophils possess potent antibacterial properties in vivo. *Infect. Immun.* 77:4976–4982. https://doi.org/10.1128/IAI.00306-09

Love, M.I., W. Huber, and S. Anders. 2014. Moderated estimation of fold change and dispersion for RNA-seq data with DESeq2. *Genome Biol.* 15:550. https://doi.org/10.1186/s13059-014-0550-8

Lowe, D.M., A.K. Bandara, G.E. Packe, R.D. Barker, R.J. Wilkinson, C.J. Griffiths, and A.R. Martineau. 2013. Neutrophilia independently predicts death in tuberculosis. *Eur. Respir. J.* 42:1752–1757. https://doi.org/10.1183/09031936.00140913

Mayer-Barber, K.D., and A. Sher. 2015. Cytokine and lipid mediator networks in tuberculosis. *Immunol. Rev.* 264:264–275. https://doi.org/10.1111/imr.12249

Mayer-Barber, K.D., B.B. Andrade, S.D. Oland, E.P. Amaral, D.L. Barber, J. Gonzales, S.C. Derrick, R. Shi, N.P. Kumar, W. Wei, et al. 2014. Host-directed therapy of tuberculosis based on interleukin-1 and type I interferon crosstalk. *Nature.* 511:99–103. https://doi.org/10.1038/nature13489

O'Garra, A., P.S. Redford, F.W. McNab, C.I. Bloom, R.J. Wilkinson, and M.P. Berry. 2013. The immune response in tuberculosis. *Annu. Rev. Immunol.* 31:475–527. https://doi.org/10.1146/annurev-immunol-032712-095939

O'Shea, M.K., T.E. Fletcher, J. Muller, R. Tanner, M. Matsumiya, J.W. Bailey, J. Jones, S.G. Smith, G. Koh, W.G. Horsnell, et al. 2018. Human Hookworm Infection Enhances Mycobacterial Growth Inhibition and Associates With Reduced Risk of Tuberculosis Infection. *Front. Immunol.* 9:2893. https://doi.org/10.3389/fimmu.2018.02893

Parikka, M., M.M. Hammarén, S.K. Harjula, N.J. Halfpenny, K.E. Oksanen, M.J. Lahtinen, E.T. Pajula, A. Iivanainen, M. Pesu, and M. Rämet. 2012. Mycobacterium marinum causes a latent infection that can be reactivated by gamma irradiation in adult zebrafish. *PLoS Pathog.* 8:e1002944. https://doi.org/10.1371/journal.ppat.1002944

Pavord, I.D., S. Korn, P. Howarth, E.R. Bleecker, R. Buhl, O.N. Keene, H. Ortega, and P. Chanez. 2012. Mepolizumab for severe eosinophilic asthma (DREAM): A multicentre, double-blind, placebo-controlled trial. *Lancet.* 380:651–659. https://doi.org/10.1016/S0140-6736(12)60988-X

Phipps, S., C.E. Lam, S. Mahalingam, M. Newhouse, R. Ramirez, H.F. Rosenberg, P.S. Foster, and K.I. Matthaei. 2007. Eosinophils contribute to innate antiviral immunity and promote clearance of respiratory syncytial virus. *Blood.* 110:1578–1586. https://doi.org/10.1182/blood-2007-01-071340

Pisu, D., L. Huang, J.K. Grenier, and D.G. Russell. 2020. Dual RNA-seq of Mtb-infected macrophages in vivo reveals ontologically distinct host-pathogen interactions. *Cell Rep.* 30:335–350.e4. https://doi.org/10.1016/j.celrep.2019.12.033

Rafi, W., R. Ribeiro-Rodrigues, J.J. Ellner, and P. Salgame. 2012. 'Coinfection-helminthes and tuberculosis'. *Curr. Opin. HIV AIDS.* 7:239–244. https://doi.org/10.1097/COH.0b013e3283524dc5

Rosenberg, H.F., K.D. Dyer, and P.S. Foster. 2013. Eosinophils: Changing perspectives in health and disease. *Nat. Rev. Immunol.* 13:9–22. https://doi.org/10.1038/nri3341

Rothchild, A.C., G.S. Olson, J. Nemeth, L.M. Amon, D. Mai, E.S. Gold, A.H. Diercks, and A. Aderem. 2019. Alveolar macrophages generate a non-canonical NRF2-driven transcriptional response *to Mycobacterium tuberculosis* in vivo. *Sci. Immunol.* 4:aaw6693. https://doi.org/10.1126/sciimmunol.aaw6693

Rothenberg, M.E., A.D. Klion, F.E. Roufosse, J.E. Kahn, P.F. Weller, H.U. Simon, L.B. Schwartz, L.J. Rosenwasser, J. Ring, E.F. Griffin, et al. Mepolizumab HES Study Group. 2008. Treatment of patients with the hypereosinophilic syndrome with mepolizumab. *N. Engl. J. Med.* 358:1215–1228. https://doi.org/10.1056/NEJMoa070812

Ruhl, C.R., B.L. Pasko, H.S. Khan, L.M. Kindt, C.E. Stamm, L.H. Franco, C.C. Hsia, M. Zhou, C.R. Davis, T. Qin, et al. 2020. Mycobacterium tuberculosis sulfolipid-1 activates nociceptive neurons and induces cough. *Cell.* 181:293–305.e11. https://doi.org/10.1016/j.cell.2020.02.026

Sallin, M.A., K.D. Kauffman, C. Riou, E. Du Bruyn, T.W. Foreman, S. Sakai, S.G. Hoft, T.G. Myers, P.J. Gardina, A. Sher, et al. 2018. Host resistance to pulmonary Mycobacterium tuberculosis infection requires CD153 expression. *Nat. Microbiol.* 3:1198–1205. https://doi.org/10.1038/s41564-018-0231-6

Shah, K., A. Ignacio, K.D. McCoy, and N.L. Harris. 2020. The emerging roles of eosinophils in mucosal homeostasis. *Mucosal Immunol.* 13:574–583. https://doi.org/10.1038/s41385-020-0281-y

Shamri, R., J.J. Xenakis, and L.A. Spencer. 2011. Eosinophils in innate immunity: An evolving story. *Cell Tissue Res.* 343:57–83. https://doi.org/10.1007/s00441-010-1049-6

Simon, H.U., S. Yousefi, N. Germic, I.C. Arnold, A. Haczku, A.V. Karaulov, D. Simon, and H.F. Rosenberg. 2020. The cellular functions of eosinophils: Collegium Internationale Allergologicum (CIA) update 2020. *Int. Arch. Allergy Immunol.* 181:11–23. https://doi.org/10.1159/000504847

Singhania, A., C.M. Graham, L. Gabryšová, L. Moreira-Teixeira, E. Stavropoulos, J.M. Pitt, P. Chakravarty, A. Warnatsch, W.J. Branchett, L. Conejero, et al. 2019. Transcriptional profiling unveils type I and II interferon networks in blood and tissues across diseases. *Nat. Commun.* 10:2887. https://doi.org/10.1038/s41467-019-10601-6

Soneson, C., M.I. Love, and M.D. Robinson. 2015. Differential analyses for RNA-seq: Transcript-level estimates improve gene-level inferences. *F1000 Res.* 4:1521. https://doi.org/10.12688/f1000research.7563.1

Straumann, A., S. Conus, P. Grzonka, H. Kita, G. Kephart, C. Bussmann, C. Beglinger, D.A. Smith, J. Patel, M. Byrne, and H.U. Simon. 2010. Anti-interleukin-5 antibody treatment (mepolizumab) in active eosinophilic oesophagitis: A randomised, placebo-controlled, double-blind trial. *Gut.* 59:21–30. https://doi.org/10.1136/gut.2009.178558

Swaim, L.E., L.E. Connolly, H.E. Volkman, O. Humbert, D.E. Born, and L. Ramakrishnan. 2006. *Mycobacterium marinum* infection of adult zebrafish causes caseating granulomatous tuberculosis and is moderated by adaptive immunity. *Infect. Immun.* 74:6108–6117. https://doi.org/10.1128/IAI.00887-06

Takaki, K., J.M. Davis, K. Winglee, and L. Ramakrishnan. 2013. Evaluation of the pathogenesis and treatment of Mycobacterium marinum infection in zebrafish. *Nat. Protoc.* 8:1114–1124. https://doi.org/10.1038/nprot.2013.068

Trauner, A., Q. Liu, L.E. Via, X. Liu, X. Ruan, L. Liang, H. Shi, Y. Chen, Z. Wang, R. Liang, et al. 2017. The within-host population dynamics of

Mycobacterium tuberculosis vary with treatment efficacy. *Genome Biol.* 18:71. https://doi.org/10.1186/s13059-017-1196-0

Travers, J., and M.E. Rothenberg. 2015. Eosinophils in mucosal immune responses. *Mucosal Immunol.* 8:464–475. https://doi.org/10.1038/mi.2015.2

van Soelen, N., A.M. Mandalakas, H.L. Kirchner, G. Walzl, H.M. Grewal, M. Jacobsen, and A.C. Hesseling. 2012. Effect of Ascaris lumbricoides specific IgE on tuberculin skin test responses in children in a high-burden setting: A cross-sectional community-based study. *BMC Infect. Dis.* 12:211. https://doi.org/10.1186/1471-2334-12-211

Veiga-Fernandes, H., and D. Mucida. 2016. Neuro-immune interactions at barrier surfaces. *Cell.* 165:801–811. https://doi.org/10.1016/j.cell.2016.04.041

Vijayan, V.K., A.M. Reetha, M.S. Jawahar, K. Sankaran, and R. Prabhakar. 1992. Pulmonary eosinophilia in pulmonary tuberculosis. *Chest.* 101:1708–1709. https://doi.org/10.1378/chest.101.6.1708

Vinhaes, C.L., D. Oliveira-de-Souza, P.S. Silveira-Mattos, B. Nogueira, R. Shi, W. Wei, X. Yuan, G. Zhang, Y. Cai, C.E. Barry III, et al. 2019. Changes in inflammatory protein and lipid mediator profiles persist after antitubercular treatment of pulmonary and extrapulmonary tuberculosis: A prospective cohort study. *Cytokine.* 123:154759. https://doi.org/10.1016/j.cyto.2019.154759

World Health Organization. 2020. Global Tuberculosis Report 2020. https://apps.who.int/iris/bitstream/handle/10665/336069/9789240013131-eng.pdf (accessed July 31, 2021).

Wolf, A.J., B. Linas, G.J. Trevejo-Nuñez, E. Kincaid, T. Tamura, K. Takatsu, and J.D. Ernst. 2007. *Mycobacterium tuberculosis* infects dendritic cells with high frequency and impairs their function in vivo. *J. Immunol.* 179:2509–2519. https://doi.org/10.4049/jimmunol.179.4.2509

Yousefi, S., J.A. Gold, N. Andina, J.J. Lee, A.M. Kelly, E. Kozlowski, I. Schmid, A. Straumann, J. Reichenbach, G.J. Gleich, and H.U. Simon. 2008. Catapult-like release of mitochondrial DNA by eosinophils contributes to antibacterial defense. *Nat. Med.* 14:949–953. https://doi.org/10.1038/nm.1855

Yu, G., and Q.Y. He. 2016. ReactomePA: An R/Bioconductor package for reactome pathway analysis and visualization. *Mol. Biosyst.* 12:477–479. https://doi.org/10.1039/C5MB00663E

Yu, C., A.B. Cantor, H. Yang, C. Browne, R.A. Wells, Y. Fujiwara, and S.H. Orkin. 2002. Targeted deletion of a high-affinity GATA-binding site in the GATA-1 promoter leads to selective loss of the eosinophil lineage in-vivo. *J. Exp. Med.* 195:1387–1395. https://doi.org/10.1084/jem.20020656

Yu, G., L.G. Wang, Y. Han, and Q.Y. He. 2012. clusterProfiler: An R package for comparing biological themes among gene clusters. *OMICS.* 16:284–287. https://doi.org/10.1089/omi.2011.0118

JEM

Supplemental material

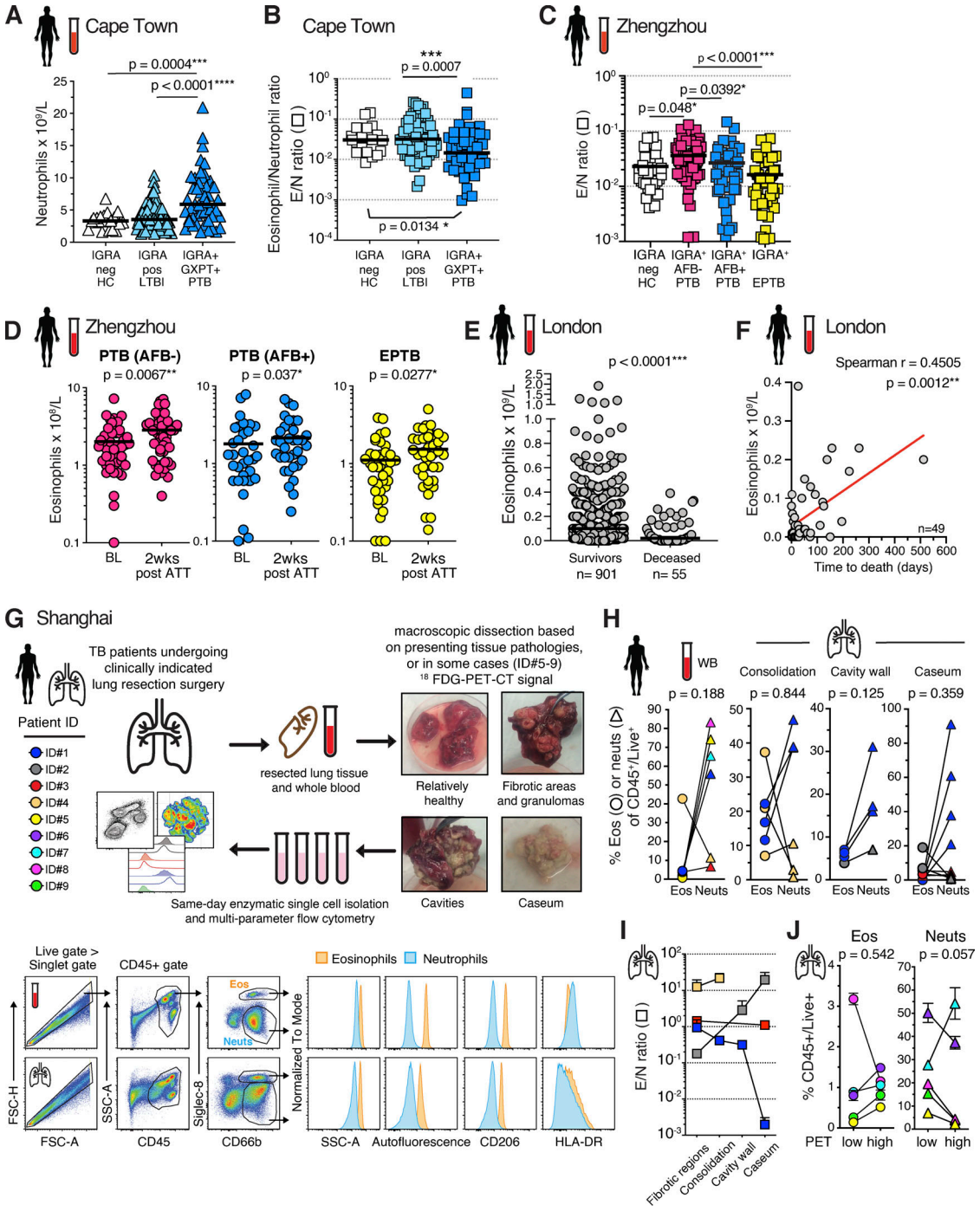

Figure S1. **Peripheral blood eosinophils in clinical cohorts and granulocyte isolation from human TB lung lesions. (A and B)** Cape Town cohort: Circulating neutrophil numbers and E/N ratio in IGRA-negative HC (n = 20), IGRA-positive individuals with LTBI (n = 77), and GXPT-positive individuals with PTB (n = 49; Kruskal–Wallis test with Dunn's correction). **(C)** Zhengzhou cohort: E/N ratio in HC (n = 30), AFB⁻ staining (sputum negative) in PTB (n = 64, pink), AFB⁺ staining (sputum positive) in PTB (n = 48, blue), and EPTB (n = 50, yellow; Kruskal–Wallis test with Dunn's correction). **(D)** Zhengzhou cohort: Circulating eosinophil numbers at baseline (BL) and 2 wk after ATT (Wilcoxon matched pairs test) from color-coded clinical groups (pink: IGRA + AFB⁻ PTB, n = 47 pairs; blue: IGRA + AFB⁺ PTB, n = 34 pairs; yellow: EPTB, n = 30 pairs). **(E)** London cohort: Circulating eosinophil numbers in survivor (n = 901) or deceased (n = 55) TB patients (Mann–Whitney test). **(F)** London cohort: Circulating eosinophil numbers correlated with time to death (n = 49, Spearman correlation test). **(G)** Schematic study overview and examples of human lung TB lesions after resection surgery (n = 9) and flow cytometric gating strategy of human lung TB lesions for eosinophil and neutrophil quantification in Shanghai cohort. **(H)** Shanghai cohort: Eosinophil (circles) and neutrophil (triangles) proportions of CD45⁺ cells depicting individual samples per patient (connecting line according to color-coded patient ID, Wilcoxon matched pairs test, two tailed). **(I)** Shanghai cohort: Summary E/N in resected human lung lesions (connecting line according to color-coded patient ID; tissues depicted as mean and SEM of n = 1–6 samples per tissue type and patient). **(J)** Shanghai cohort: Eosinophil and neutrophil proportions of CD45⁺ cells in ¹⁸FDG PET/CT low- or high-signal intensity (SUV_{max} >5.0) lung lesions (connecting line according to color-coded patient ID, n = 5, two-tailed Wilcoxon matched pairs test). Eos, eosinophils; FSC, forward scatter; Neuts, neutrophils; SSC, side scatter.

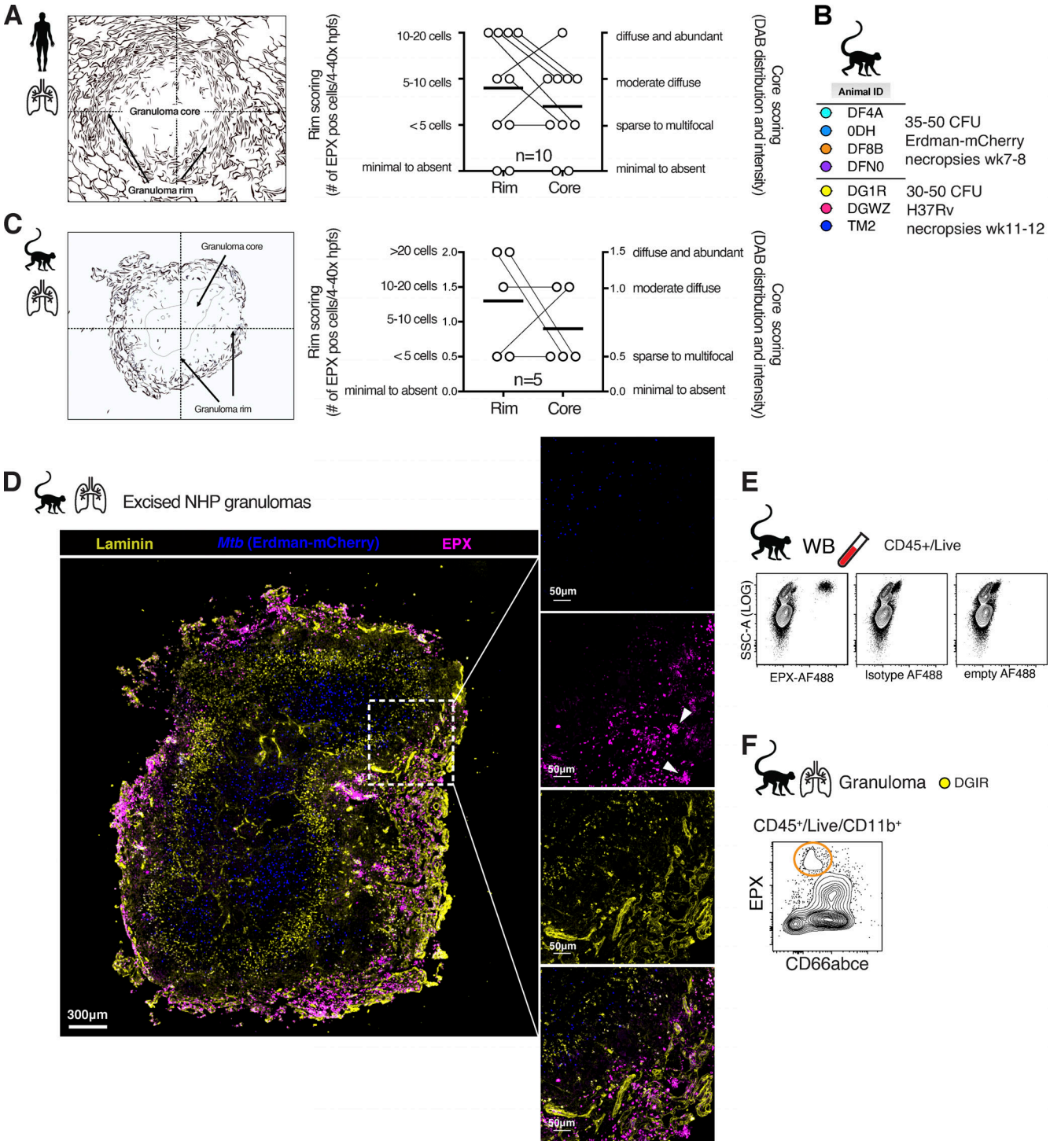

Figure S2. **Human and NHP TB lesions assessed by H&E and EPX immunohistological and flow cytometric staining. (A)** Rome cohort: Histological scoring of eosinophil distribution in human TB lesion on blinded specimens (n = 10). **(B)** Animal IDs and infection dose and strains for NHP *Mtb* infections (male and female, n = 7, two independent experiments). **(C)** Granuloma outline and legend for histological scoring of NHP granulomas on blinded specimens (n = 5). **(D)** EPX immunofluorescence staining on thin sections from paraffin-embedded granulomas after Erdman-mCherry (blue) *Mtb* infection. **(E)** Isotype and fluorescence minus one (empty) control of EPX–AF488 staining in NHP WB. **(F)** Example EPX FACS staining in granulomas from rhesus macaques. DAB, 3,3′-diaminobenzidine; hpfs, high-power fields; SSC, side scatter.

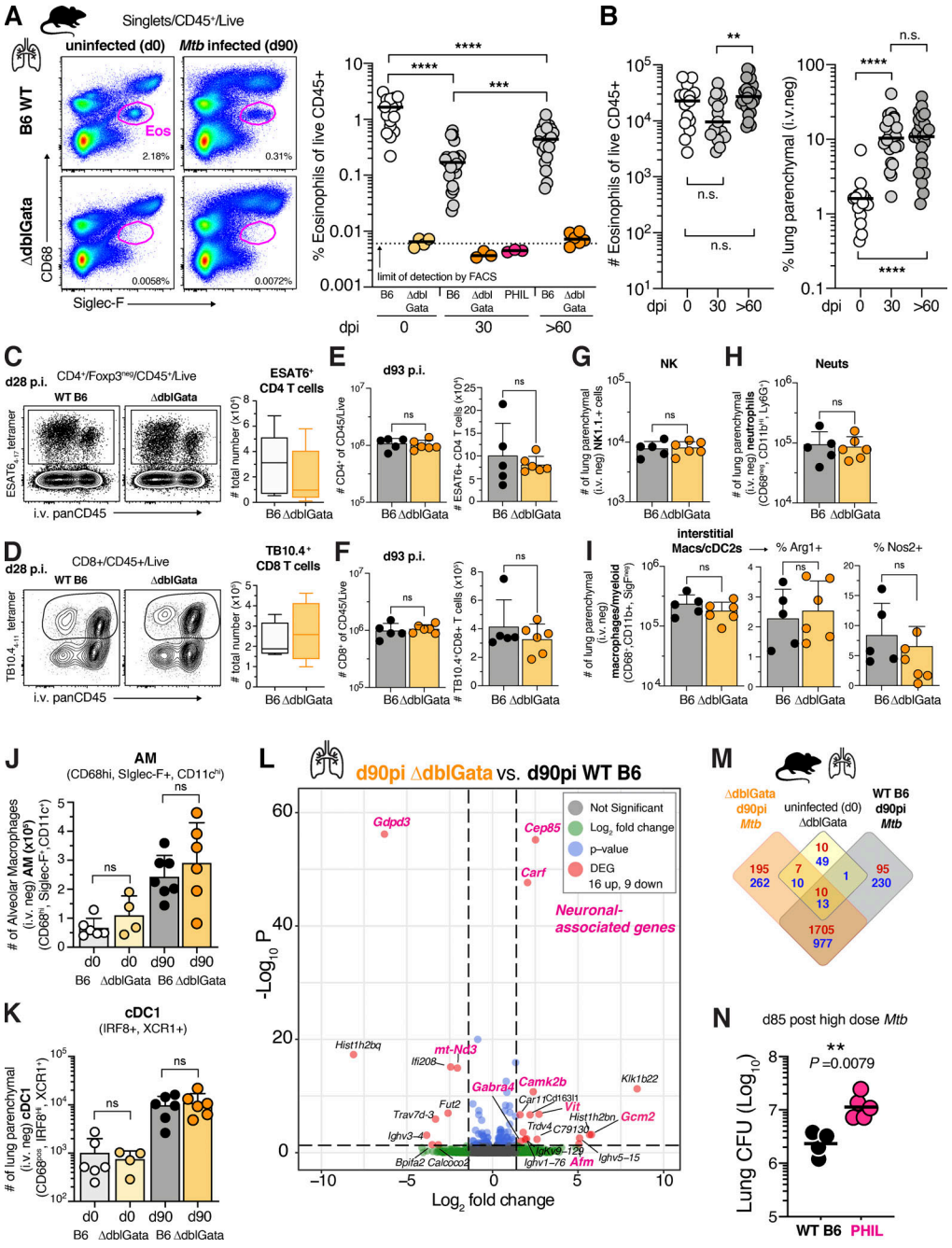

Figure S3. **Transcriptional changes and immune profiling in eosinophil-deficient mice after *Mtb* infection. (A)** Example flow cytometry of eosinophils in B6 WT and ΔdblGata mice and lung eosinophil frequency in naive and *Mtb*-infected (100–300 CFU) B6 WT and eosinophil-deficient mice (male and female, n = 3–28, one to four independent experiments per time point, Mann–Whitney test). **(B)** Numbers of total and lung parenchymal (i.v.^{neg}) eosinophils at indicated time points after *Mtb* infection (male and female, n = 12–25, three to four independent experiments per time point, Mann–Whitney test). **(C and D)** Representative flow cytometry for intravascular stain and ESAT6$_{4-17}$ CD4 tetramer with quantification of *Mtb*-specific CD4$^+$ T cells and *Mtb*-specific CD8$^+$ T cells 4 wk after infection (male and female, n = 8–10, two experiments, Mann–Whitney test). **(E and F)** Quantification of total CD4$^+$ cells and ESAT6$_{4-17}$ CD4 tetramer-positive CD4$^+$ T cells and total CD8$^+$ and TB10.4$_{4-11}$-specific CD8 tetramer-positive cells 3 mo after infection (male and female, n = 5–6, two experiments, Mann–Whitney test). **(G–I)** Quantification at 3 mo after infection of Nk1.1$^+$ cells, neutrophils, and interstitial macrophages (Macs)/DC2 and their corresponding frequency of arginase (Arg1) or inducible nitric oxide synthase (Nos2) expression (male and female, n = 5–6, two experiments, Mann–Whitney test). **(J and K)** Quantification at baseline and 3 mo after infection of alveolar macrophages (AM) and XCR1$^+$ conventional DC1 (cDC1; female, n = 4–6, one experiment, Mann–Whitney test). **(L)** Volcano plot of DEGs (red) between lungs of d90 WT (n = 4) or B6 ΔdblGata (n = 5) *Mtb*-infected mice. Green represents genes with log$_2$ fold change ±1.4, blue represents genes with a P value and FDR <0.05, and gray represents genes that are not significant. The changes in gene expression levels were considered significant when statistical test values (FDR-adjusted P value) were <0.05 and the fold change/difference higher than ±1.4. Neuronal-associated genes are annotated in pink (n = 4–5 per group, one experiment). **(M)** Venn diagram of DEGs in lungs from 3-mo (d90)–infected WT B6 (n = 4) or B6 ΔdblGata mice (n = 5) and uninfected (d0) B6 ΔdblGata (n = 4) compared with lungs from uninfected (d0) WT B6 mice (n = 5). Upregulated DEGs are shown in red and downregulated DEGs in blue (n = 4–5 per group, one experiment). **(N)** Lung bacterial loads 85 d after high-dose *Mtb* infection in eosinophil-deficient B6 PHIL mice (male, n = 4–5, one experiment, Mann–Whitney test).

Table S1, provided online as a separate Excel file, lists RNA sequencing analysis results of DEGs, modules, and GSEA.